Available on CMS information server **CMS CR 1998/004**

CMS Conference Report

4th February 1998

A Pedagogical Introduction to the CMS Electromagnetic Calorimeter

D. Barney

CERN, Geneva, Switzerland

ECAL Group

CMS collaboration

Abstract

Physics at the LHC requires extremely high performance detectors. The CMS electromagnetic calorimeter ('ECAL') has been designed to facilitate the discovery of the Higgs boson, thought to be responsible for the spontaneous symmetry breaking observed in the electroweak sector of the Standard Model. This report outlines the particular physics requirements that govern the choice and design of the CMS ECAL and describes in some detail the properties of the Lead Tungstate crystals used in the ECAL, the readout system and the Preshower detectors. Testbeam results are presented which illustrate the progress that has been made during the past few years and which highlight the features of the CMS ECAL.

Presented at *The Actual Problems of Particle Physics*, Gomel, Belarus 8-16th August 1997

1 Introduction

This report is intended to be a pedagogical introduction to the design features of the CMS ECAL. The target audience was a group of theoretical particle physics students from the Commonwealth of Independent States. With a view to this audience, an introduction (section 2) to the basics of electromagnetic calorimetry is first given, which introduces the physical quantities important for the choice of a good calorimeter medium. Section 3 then outlines the physics goals of CMS, in particular the discovery of the Higgs boson. Attention is paid to the possibility of an 'intermediate mass' Higgs (between about 80 GeV and 135 GeV) as its 'gold-plated' discovery channel is the decay to two photons; this decay imposes strict criteria on the design of the ECAL. Section 4 describes the physical and optical characteristics of the lead tungstate ($PbWO_4$) crystals, whilst section 5 briefly overviews the photodetectors and readout electronics. There are two Preshower detectors in CMS, one in the barrel and one in the endcaps, although only the endcap preshower is a baseline item; they have similar structures but perform different functions: photon angular measurement in the barrel; neutral pion rejection in the endcaps. These detectors are described in section 6. Finally, testbeam results showing progress during the past few years are given in section 7.

The majority of the information found in this report can also be found, in more detail, in the CMS ECAL Technical Design Report [1].

2 Introduction to Electromagnetic Calorimeters

Each sub-detector in a high energy physics experiment is optimized for the detection and measurement of a specific type of particle. Electromagnetic calorimeters measure the *energy* of electrons and photons. They also aid in particle identification (specifically electron/charged-pion separation in conjunction with the tracker) and help to measure the energy of high energy hadrons (in conjunction with the hadron calorimeter - HCAL).

2.1 Detection Mechanism

When a high energy photon or electron is incident upon a dense medium it may initiate an 'electromagnetic shower', via the processes of bremsstrahlung, pair-production and, at low energies, Compton scattering. The electrons/positrons in the shower may produce either ionization or 'light' (or both), depending on the material in which the shower occurs. Calorimeters based upon ionization detection are not discussed in this report.

Light may be produced in three different ways:

1. Separate shower media and scintillators - e.g. lead+scintillator 'sandwich' [2]. The shower develops in the lead and the produced electrons/positrons create scintillation in layers of scintillator.
2. Čerenkov light [3] inside a dense medium such as lead glass [4] or lead fluoride (PbF_3).
3. Scintillation light [5] inside the shower medium - e.g. caesium iodide or lead tungstate.

The produced light is then passed, perhaps via light-guides, to photodetectors such as photomultiplier tubes (PMTs) or silicon photo-diodes.

Figure 1 shows a simulation of a typical electromagnetic shower produced inside lead tungstate crystals from an incident 10 GeV electron. The spread of the shower in both the longitudinal and transverse directions is dependent upon many factors, including some physical properties of the shower medium and the energy of the incident particle. In this diagram three crystals are shown; each measures about 23cm in length and has a transverse dimension of just over 2cm - see section 4. The 'produced' scintillation light is not shown.

2.2 Physical Quantities Relevant for Shower Media

A variety of different shower media have been used in high energy physics experiments. The appropriate choice depends upon the particular application - resolution, cost, space requirements etc. The principle physical characteristics which govern the choice are as follows:

- **Radiation length - X_0** - the longitudinal distance over which an electron loses (1-1/e) of its energy by bremsstrahlung; about 25 X_0 of material is required in order to contain (longitudinally) about 99% of the shower. An approximate form relating X_0 to a specific element with atomic number Z, atomic mass A and density ρ is given

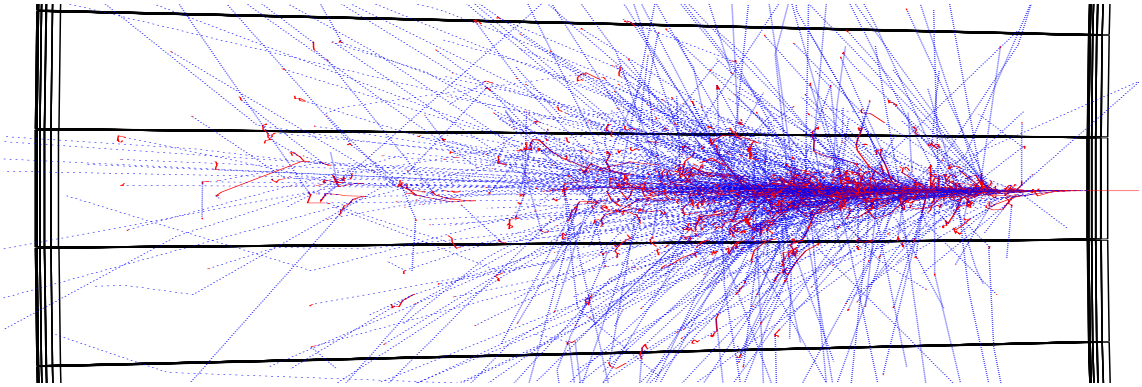

Figure 1: Simulation of a 10 GeV electron incident (from the right) on lead tungstate crystals. The photodetectors would be on the left (but not shown). The dashed lines represent photons produced by electron/positron bremsstrahlung; short solid lines represent the electrons and positrons created by pair-production.

in equation 1 below.

$$X_0(cm) = \frac{716.4A}{\rho Z(Z+1)ln(287/\sqrt{Z})} \tag{1}$$

For a mixture or compound this becomes:

$$1/X_0 = \sum w_j/X_j \tag{2}$$

where w_j and X_j are the fraction by weight and the radiation length for the jth element.

- **Molière radius - $\mathbf{R}_M$** - the scale for the transverse spread of an electromagnetic shower. It is related to X_0 by equation 3 below.

$$R_M = X_0 E_s/E_c \tag{3}$$

where $E_s \approx 21$ MeV and E_c is the *critical energy* defined by Rossi [6] as the energy at which ionization loss per radiation length is equal to the electron energy.

- **$\mathbf{N}_{pe}$** - Amount of detected light per unit energy deposited.
- **Wavelength(s) of light emitted in shower** - important for the choice of photodetector.
- **$\mathbf{T}_{scint}$** - Scintillation emission time (if relevant).

Table 1 gives the values of these quantities for some shower media. These will be discussed further in section 4.

				Light Emission		
				Čerenkov	**Scintillation**	
Material	**X_0 (cm)**	**R_M (cm)**	**Light output (relative for scintillators)**	**Peak λ (nm)**	**Peak λ (nm)**	**Emission time (ns)**
Lead	0.56	1.22	-	-	-	-
Lead Glass	2.8	3.2	290 γ/cm	>500	-	-
NaI	2.59	4.8	1.00	-	410	230
BGO	1.12	2.3	0.18	-	480	300
CsI	1.85	3.5	0.20	-	315	16
CeF_3	1.68	2.6	0.08	-	340	25
$PbWO_4$	0.89	2.2	0.01	-	440	5-15

Table 1: Physical characteristics of some shower media used in electromagnetic calorimeters.

2.3 Types of Electromagnetic Calorimeter

The two principle types of light-detecting electromagnetic calorimeter are shown in figures 2 and 3.

Sampling: The calorimeter is divided into alternate 'sheets' of dense shower media and light producer. For example, a common setup is to use layers of lead (or depleted uranium) interspersed with plastic scintillator. The shower develops in the lead layers; electrons/positrons from the shower which pass through the plastic produce scintillation light which is then detected.

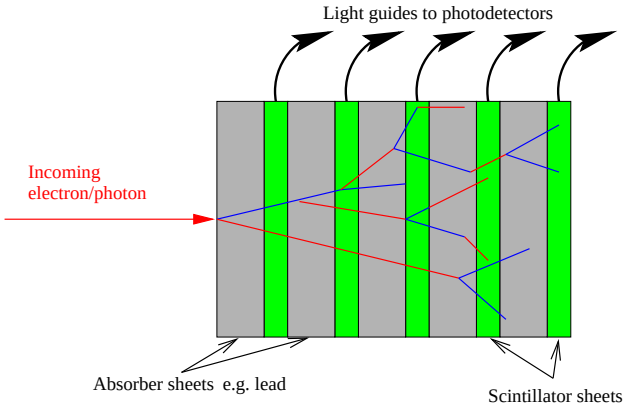

Figure 2: Schematic representation of a sampling calorimeter, comprising lead sheets (shower media) and scintillators (light producers)

Homogeneous: One substance acts as both shower medium and light producer. The light may be either scintillation (as in CsI and $PbWO_4$ for example) or Čerenkov. This light can then be detected.

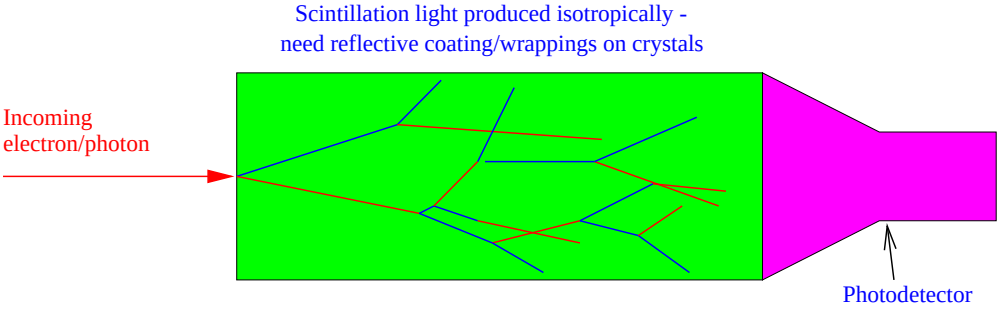

Figure 3: Schematic representation of a homogeneous calorimeter

2.4 The Energy Resolution Equation

The ultimate aim of an electromagnetic calorimeter is to measure the energy of photons/electrons as well as possible. The energy resolution can be approximated by equation 4.

$$\frac{\sigma_E}{E} = \frac{a}{\sqrt{E}} \oplus \frac{\sigma_N}{E} \oplus c \tag{4}$$

where:

E is the energy, usually in GeV

$\frac{\sigma_E}{E}$ is the energy resolution

a is the "stochastic" term - mainly governed by photostatistics and sampling fluctuations

σ_N is the "noise" term - electronics noise and pileup

c is the "constant" term - mainly from shower containment limitations and calorimeter non-uniformities

$\oplus$ implies a quadratic sum

For optimum calorimeter performance each term should be small and of the same order at the relevant electron/photon energies.

2.5 Relative Merits of Sampling and Homogeneous Calorimeters

If we assume a Higgs mass of about 100 GeV (relevant for $H \longrightarrow \gamma\gamma$ searches) then the typical photon energy will be of the order of about 50 GeV (in the barrel) and about 180 GeV (in the endcaps - due to the Lorentz boost). The average photon energy of relevance may then be approximated to about 100 GeV.

Sampling Calorimeters

It is difficult to obtain a stochastic term below about 10% without demanding strict mechanical tolerances. This sets the scale of the constant term to be $\leq$1% and the noise term to be equivalent to about 500 MeV.

Homogeneous Calorimeters

These have the potential to achieve stochastic terms of $\approx$ 2% due to much smaller sampling fluctuations. In this case the limitation is the control of systematics which build up the constant term, which needs to be around 0.5%.

The expected energy resolution of a $PbWO_4$ calorimeter is:

$$\frac{\sigma_E}{E} = \frac{2\%}{\sqrt{E}} \oplus \frac{\approx 200MeV}{E} \oplus 0.5\% \tag{5}$$

3 Physics Requirements

In this section the design requirements of the electromagnetic calorimeter are summarised. The design is driven by the physics goals of CMS which will be reviewed briefly. Particular attention is paid to the two-photon decay of the intermediate Higgs boson as this channel is extremely demanding of the electromagnetic calorimeter.

3.1 Reminder of CMS Design Philosophy

At this point it is useful to recall the CMS design goals:

1. A very good and redundant muon system
2. The best possible electromagnetic calorimeter consistent with 1.
3. A high quality central tracker to complement 1. and 2.
4. A financially affordable detector

The detector should thus be optimized for leptons and photons, facilitating the detection of the Higgs through various decay channels.

3.2 Terminology

The following definitions will be used throughout the remainder of this section and those subsequent:

- 1 year at low luminosity (10^{33}cm^{-2}s^{-1}) $\equiv 10^4$pb^{-1}
- 1 year at high luminosity (10^{34}cm^{-2}s^{-1}) $\equiv 10^5$pb^{-1}

and for the co-ordinate system:

- The beam axis will be called 'Z'

- The vertical axis (with respect to 'Z') will be called 'Y'
- The horizontal axis (with respect to 'Z') will be called 'X'
- The azimuthal angle is 'ϕ'
- The polar angle is 'θ'
- The pseudorapidity ('η') is in the '$Z-\theta$' plane

3.3 Physics Goals

3.3.1 Standard Model (SM) Higgs

The principle goal of both CMS and ATLAS is the discovery (or not) of the Higgs boson. The Standard Model Higgs should have a mass between about 80 GeV/c^2 [1)] and 1 TeV/c^2 [2)]. Figure 4 shows diagramatically the 'gold-plated' decays of the Standard Model Higgs as a function of its mass.

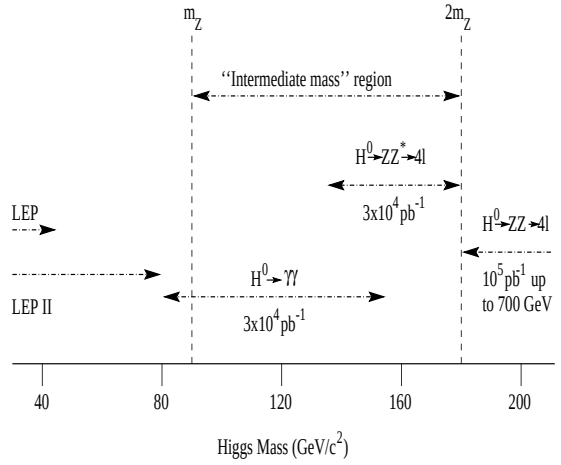

Figure 4: The 'gold-plated' decays of the Standard Model Higgs

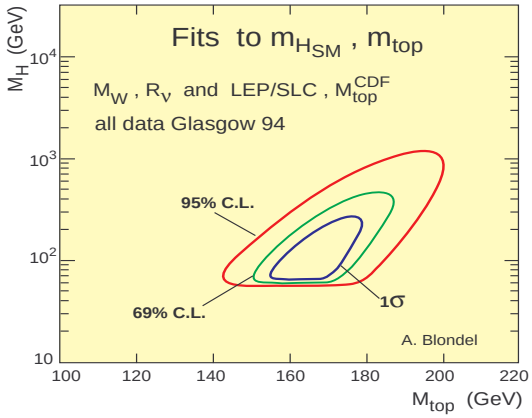

Figure 5: χ^2 as a function of m_H (m_{top} = 165 GeV/c^2) for precision electroweak data interpreted within the SM radiative corrections framework

The discovery range for the Standard Model Higgs can be extended up to the 1 TeV limit by detecting forward jets from WW and ZZ fusion and exploiting decay channels with large branching ratios (e.g. $H^0 \longrightarrow WW \longrightarrow l\nu jj$ and $H^0 \longrightarrow ZZ \longrightarrow lljj$).

It is important to note that many of the decay channels involve leptons and/or photons; consequently the electromagnetic calorimeter will play a leading rôle in the discovery of a Standard Model Higgs.

Current electroweak measurements point to a Standard Model Higgs with a relatively low mass, around 100 GeV/c^2. Figure 5 shows the χ^2 of various measurements as a function of the Higgs mass. The data are a few years old now, as exemplified by the mass of the top quark used (165 GeV/c^2), but are still consistent with the most recent measurements.

Figure 6 depicts the four processes responsible for Standard Model Higgs production at the LHC.

The most probable means of production is the gluon-gluon fusion mechanism, which is also the cleanest. The processes involving the vector bosons are much less probable, as shown in figure 7 which shows the predicted number of Higgs' produced per year of high luminosity running at the LHC.

The natural width of an intermediate mass SM Higgs boson is predicted to be less than 10 MeV (see figure 8). This means that the Higgs mass resolution will be entirely dominated by the detector resolution.

The most stringent requirements imposed on the ECAL are from the two-photon decay of the intermediate mass Higgs boson.

[1)] This lower limit is due to the reach of the current colliders - the Tevatron at Fermilab and LEP at CERN

[2)] Set by the constraints of unitarity

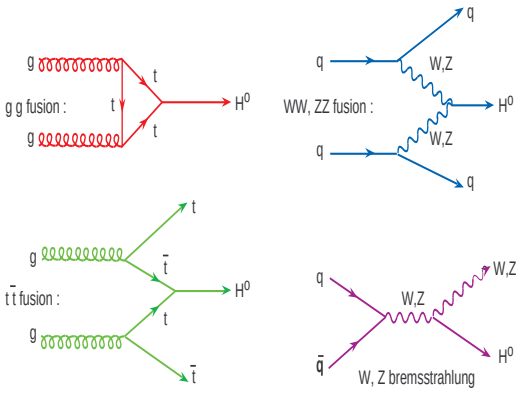

Figure 6: Standard Model Higgs production mechanisms at LHC

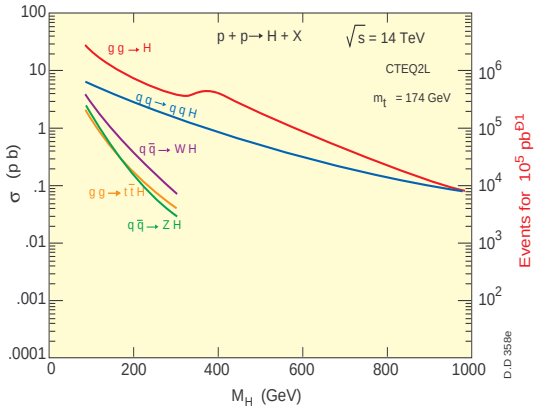

Figure 7: Cross-section and predicted number of Higgs events per years running at LHC

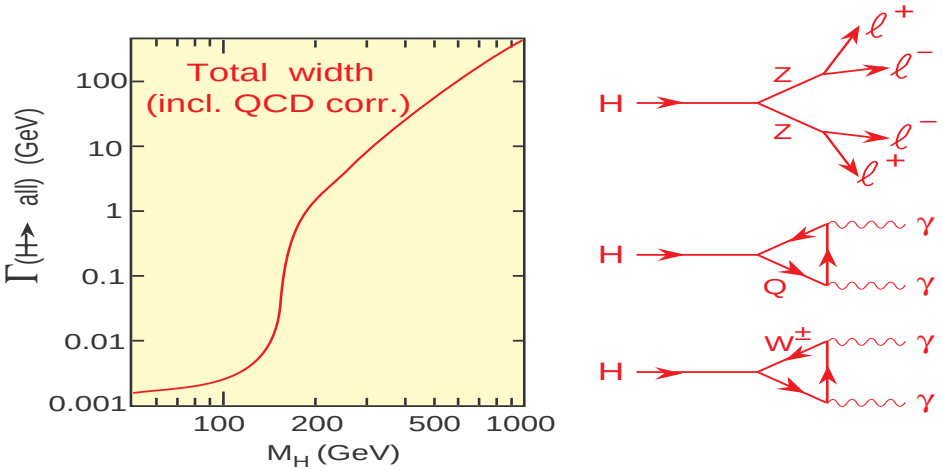

Figure 8: The natural width of the Standard Model Higgs as a function of its mass. Also shown are Feynman diagrams depicting the decays to two photons and four leptons.

Figure 8 shows the natural width of the Higgs as a function of its mass, together with three simple Feynman diagrams depicting the two-photon and four-lepton decay modes [3)] which are relevant for Higgs masses below about 200 GeV/c^2. The branching ratios for various decay modes are shown in figure 9 as a function of the Higgs mass.

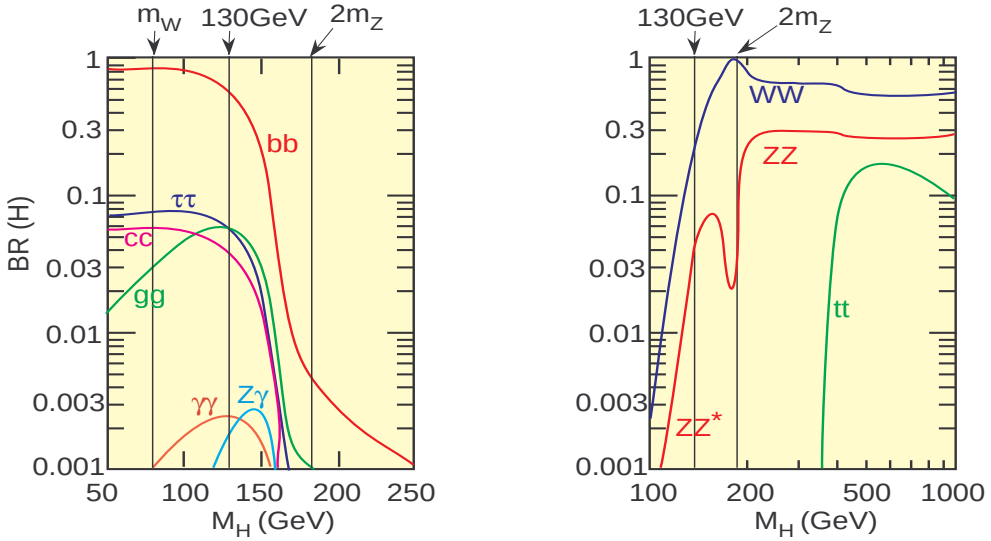

Figure 9: Branching ratios for the main decay channels of the Standard Model Higgs as a function of its mass.

It is clear that the dominant decay mode is to $b\bar{b}$ pairs but this is extremely difficult to detect efficiently. The two-photon decay (relevant for Higgs masses between about 90 GeV/c^2 and 160 GeV/c^2) is rare but is very clean. For Higgs masses above about 140 GeV/c^2 the decay to ZZ^* (subsequently decaying to four leptons) becomes important (and above $2m_Z$ the decay to two real Z's).

3.3.2 Minimal Supersymmetric Model (MSSM) Higgs

Figure 10 shows the CMS '5σ' contours in the $m_A - tan\beta$ plane for a variety of decays of supersymmetric Higgs particles. It is apparant that a large region of the parameter space will be covered - the shaded area shows the region of parameter space which cannot be covered.

Again it should be emphasised that many of the decay channels involve leptons and/or photons.

3.3.3 Other SUSY Searches

Events with many high energy jets and missing transverse energy (E_t) are the most obvious (and model independent) signatures in searches for squarks and gluinos. Hermeticity of the calorimeters is thus of the utmost importance.

3.3.4 B Physics

With an integrated luminosity of about 10^4pb^{-1} CMS is sensitive to values of $\sin 2\beta \geq 0.05$ and $\sin 2\alpha \geq 0.06$. These should be measured via the decay channels $B_d^0 \longrightarrow J/\psi K_s^0$ and $B_d^0 \longrightarrow \pi\pi$ respectively. Time development of $B_s^0 \Longleftrightarrow \bar{B}_s^0$ oscillations will enable the mixing parameter x_s to be measured for values up to 20-25.

3.3.5 Heavy Ion Physics

In addition to colliding protons, the LHC will also be able to collide heavy ions at $\sqrt{S} = 5.5$ TeV per nucleon pair. A strong suppression of the production of Υ' and Υ'' relative to Υ (when compared to pp collisions) will signal the formation of the quark-gluon plasma.

[3)] for a Higgs mass above about 140 GeV/c^2 and below $2m_Z$ one of the Z bosons in the four-lepton diagram should be replaced by a Z^*

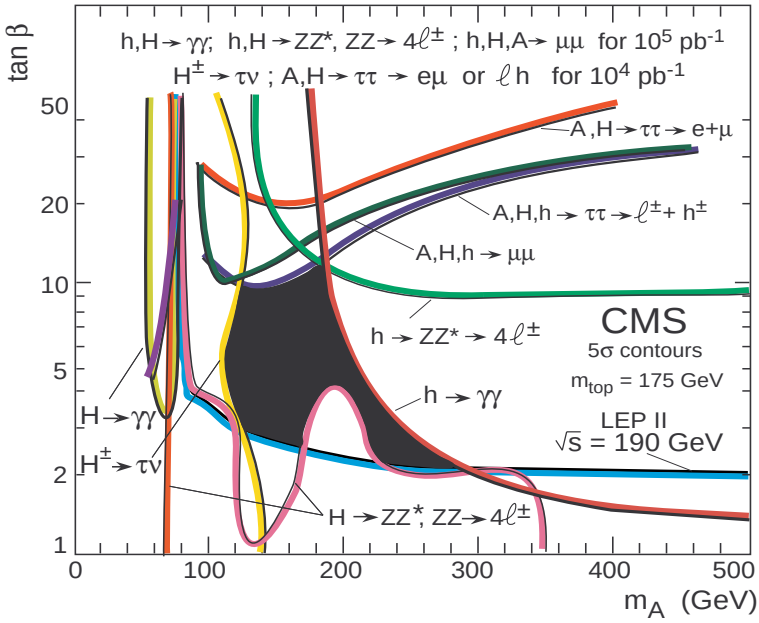

Figure 10: CMS 5σ contours for various decays of a Higgs particle within the Minimal Supersymmetric Model

3.4 The Intermediate Mass Higgs - 85 GeV/c^2 $< m_H <$ 180GeV/c^2

As mentioned previously, the measured width of an intermediate mass SM Higgs boson is entirely dominated by the detector performance.

In this case the mass resolution is given by:

$$\frac{\sigma_m}{m} = \frac{1}{2}[\frac{\sigma_{E1}}{E1} \oplus \frac{\sigma_{E2}}{E2} \oplus \frac{\sigma_\theta}{\tan(\theta/2)}] \tag{6}$$

where:

- $\frac{\sigma_m}{m}$ is the mass resolution
- $\frac{\sigma_{E1}}{E1}$ and $\frac{\sigma_{E2}}{E2}$ are the energy resolutions for the two photons
- θ is the angle (in radians) between the two photons
- σ_θ is the angular resolution

In addition to the requirement that the terms in the mass resolution be kept small the design of an appropriate ECAL is also dictated by the necessities of background rejection, geometric acceptance and radiation tolerance.

3.4.1 Energy Resolution Requirements

For illustration purposes we can assume a Higgs mass of 100 GeV/c^2. In this case the following kinematic cuts would be applied to two-photon events in CMS:

$$P_t^{\gamma_1} > 40GeV \qquad P_t^{\gamma_2} > 25GeV \qquad |\eta| < 2.5 \tag{7}$$

The mean photon energy in the central barrel region ($|\eta| < 0.5$) would thus be around 50 GeV. If we require the ECAL constant term to be 0.5% then the stochastic and noise terms in the barrel should be around $2\%/\sqrt{E}$ and 150 MeV respectively.

In the outer part of the endcaps ($1.5 < |\eta| < 2.0$) the mean photon energy is around 140 GeV, whilst the minimum photon energy is around 80 GeV. This means that, keeping the same noise and constant terms, a higher stochastic term is acceptable (around $5\%/\sqrt{E}$).

3.4.2 Angular Resolution

In order to not dominate the mass resolution, the angular resolution should be around $50mrad/\sqrt{E}$. The angular measurement requires the photon incidence positions on the ECAL to be measured accurately, and for the primary vertex position to be known. The photon incidence positions can be measured by the ECAL itself to a good accuracy (see section 7). The largest uncertainty is in the measurement of the primary vertex position along the beam axis ('Z'): the bunches of protons have very small lateral dimensions but have a longitudinal rms spread of about 5.3cm.

In the low luminosity phase of CMS the hard tracks associated with the production of the Higgs allows the primary vertex position (along 'Z') to be measured.

However, in the high luminosity running there will be around 17 events per bunch crossing, which may make the measurement of the primary vertex position virtually impossible. If the primary vertex position is not known, the contribution to the mass resolution could be around 1.5 GeV for a 100 GeV/c^2 Higgs, a factor of about 3 higher than the mass resolution at low luminosity. In this case it may be necessary to install a barrel preshower for the angle measurement at high luminosity - see section 6.

3.4.3 Backgrounds to $H \longrightarrow \gamma\gamma$

As shown in section 3.3.1, $H \longrightarrow \gamma\gamma$ is a relatively rare decay (branching ratio $\approx 10^{-3}$ for $m_H < 150$ GeV/c^2) and has some large backgrounds. Diagrams depicting the four most important backgrounds are shown in figure 11. Isolation cuts can reduce the bremsstrahlung and jet backgrounds by a large factor, but an additional rejection factor of about 3 is required for the jet background so that it does not dominate the irreducible backgrounds. In the barrel of CMS the rejection of π^0s in jets which fake single photons can be performed by the crystals due to the relatively large separation between the two photons from the π^0. In the endcaps the separation is much smaller, necessitating a fine-granularity preshower detector - see section 6.

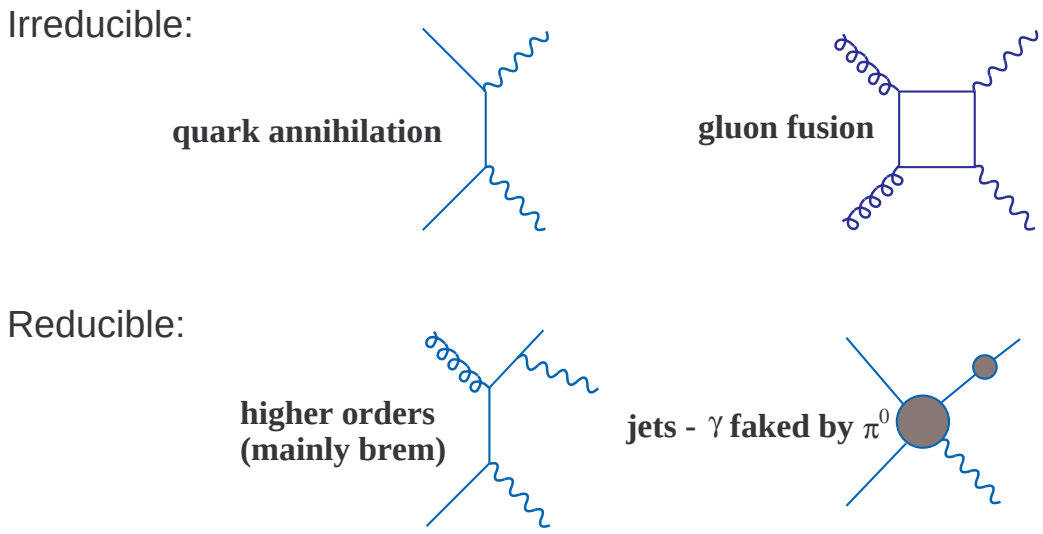

Figure 11: The principle backgrounds to the two-photon decay of the Higgs

Table 2 summarises the signal and background cross sections for the $H \longrightarrow \gamma\gamma$ decay channel, assuming an ECAL with the energy resolution terms given in section 2.5.

The degradation in mass resolution in going from low to high luminosity is mainly due to the necessary presence of the barrel preshower which degrades the energy resolution somewhat.

The background due to jets, specifically π^0s in jets faking single photons, was not included in the table. There

Signal	m_H 110 GeV/c^2	m_H 130 GeV/c^2	Background $d\sigma/dm_{\gamma\gamma}(fb/GeV)$	$m_{\gamma\gamma}$ 110 GeV/c^2	$m_{\gamma\gamma}$ 130 GeV/c^2
$\sigma \cdot B(H \longrightarrow \gamma\gamma)$ (fb)	75.9	68.3	**Quark annihilation**	61.0	41.2
Acceptance	57%	63%	**Gluon fusion**	72.4	42.4
$\sigma_m low\mathcal{L}$ (MeV)	475	600	**Isolated bremsstrahlung**	84.4	50.4
$\sigma_m high\mathcal{L}$ (MeV)	870	960	**TOTAL (isolated)**	217.8	134.0

Table 2: (a) Signal cross-section, acceptance and mass resolution at m_H=110 and m_H=130 GeV/c^2, (b) background cross-sections after cuts.

are very large theoretical uncertainties in calculating the magnitude of this background such that we require the predicted level (after cuts) to be less than the irreducible background. As mentioned previously, isolation cuts can reduce this background by a factor of about 3, and a highly segmented ECAL can provide a further factor of 3 in the barrel.

3.4.4 Geometric Acceptance and Radiation Dose

It should be noted that several important physics channels, particularly the SM Higgs decays and various SUSY channels, require an extremely hermetic ECAL. The coverage at high η is limited by the radiation dose which would be received. At $|\eta| > 2.6$, for an integrated luminosity of $5 \times 10^5 pb^{-1}$ (corresponding approximately to the first ten years of running at the LHC) the ECAL would receive a dose of > 7 Mrad and a neutron fluence of $> 2 \times 10^{14}$n/cm^2. The calorimeter medium, electronics, readout etc. have to be able to survive in this extremely hostile environment.

3.5 Contributions to the Di-photon Mass Resolution

Assuming that an electromagnetic calorimeter can be made to fulfill the criteria mentioned in the previous sections, the contributions to the di-photon mass resolution for a Higgs of 110 GeV/c^2 are as given in table 3.

Effect	Contribution, in MeV, to mass resolution for m_H = 110 GeV			
	Low Luminosity $\mathcal{L} = 10^{33} cm^{-2} s^{-1}$		High Luminosity $\mathcal{L} = 10^{34} cm^{-2} s^{-1}$	
Stochastic Term	2.0%	150	0.5%	400
Constant Term	0.5%	350	0.5%	350
Energy equivalent of noise		200		200
Angular measurement in range $\|\eta\| < 1.1$	using tracks	200	50 mrad/$\sqrt{E}$	625
Energy pileup		-		200
TOTAL		**475**		**870**

Table 3: Contributions to the di-photon mass resolution at low and high luminosity

An homogeneous electromagnetic calorimeter made from single crystals can achieve these goals.

Figure 12 shows the background subtracted di-photon spectra for Higgs masses of 90, 110, 130 and 150 GeV/c^2 for one years running at high luminosity. Also shown, in figure 13 are signal significance contours: it is apparent that the signal will have a significance greater than 5 for a majority of the intermediate mass range.

4 The CMS $PbWO_4$ Crystal Calorimeter

This section describes the physical and optical properties of lead tungstate - $PbWO_4$ - crystals, which have been chosen as the active medium for the CMS electromagnetic calorimeter. Some recent measurements concerning light yield, radiation tolerence and energy resolution are given. A brief description of the current mechanical construction is also presented.

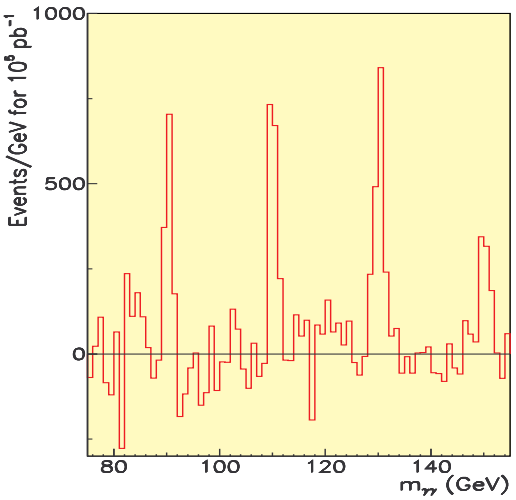

Figure 12: Background subtracted di-photon mass plot for 10^5pb^{-1} with signals at m_H = 90, 110, 130 and 150 GeV/c^2 in the CMS $PbWO_4$ calorimeter

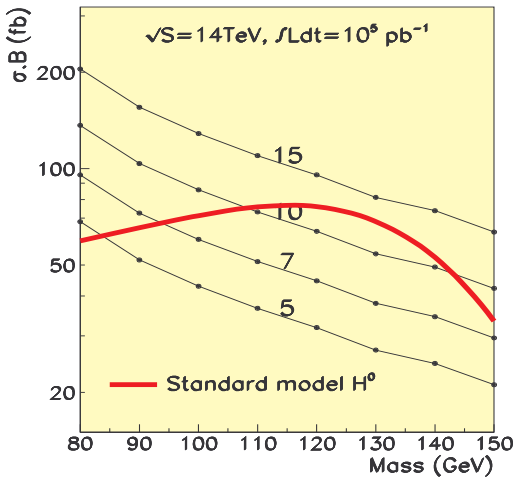

Figure 13: Signal significance contours for 10^5pb^{-1} taken at high luminosity

4.1 Shower Media Physical Quantities Revisited - with Reference to $PbWO_4$

Section 2.2 described how the physical properties of a shower medium affect the performance of an electromagnetic calorimeter. The following is a summary of the attractive properties of $PbWO_4$.

- $\mathbf{X}_0$ - this should be as short as possible to allow a compact calorimeter. For $PbWO_4$ the radiation length is 0.89cm which means only 23cm of crystal are needed for 'full' longitudinal shower containment. This results in:
  - lower cost per unit area (c.f. CeF_3 which would need 42cm long crystals and which costs approximately the same as $PbWO_4$ *per unit volume*)
  - ability to place the whole calorimetry (including the hadron calorimeter) inside the superconducting solenoid of CMS
- $\mathbf{R}_M$ - a small Molière radius allows a high granularity detector to be made at a small radius. For $PbWO_4$ this is about 2.2cm.
  - less crystals needed to laterally contain a shower - improves isolation efficiency and reduces pileup
  - excellent spatial precision - useful for angular resolution

Figure 14 shows a view of the CMS detector. The compact design is a direct consequence of the short length of the $PbWO_4$ crystals.

- **Light emission time** - should be as short as possible. Most of the light from $PbWO_4$ is emitted within 25ns, as demonstrated in figure 15. This is advantageous since we require that as few time samples are used as possible to reduce noise.
- **Amount of light output** - as much as possible. This is relatively low for $PbWO_4$
  - amplification can introduce noise
  - standard amplifying photodetectors (e.g. PM tubes) cannot operate satisfactorily in a magnetic field of 4T

  These problems have been largely overcome with the progress made on silicon avalanche photodiodes (APDs) - see section 5.

  Figure 16 shows the light yield in photoelectrons per MeV (p.e./MeV) deposited for 20 crystals produced in Bogoroditsk in 1997. The measurements were made using a PM tube. The mean value of 12.5 p.e./MeV

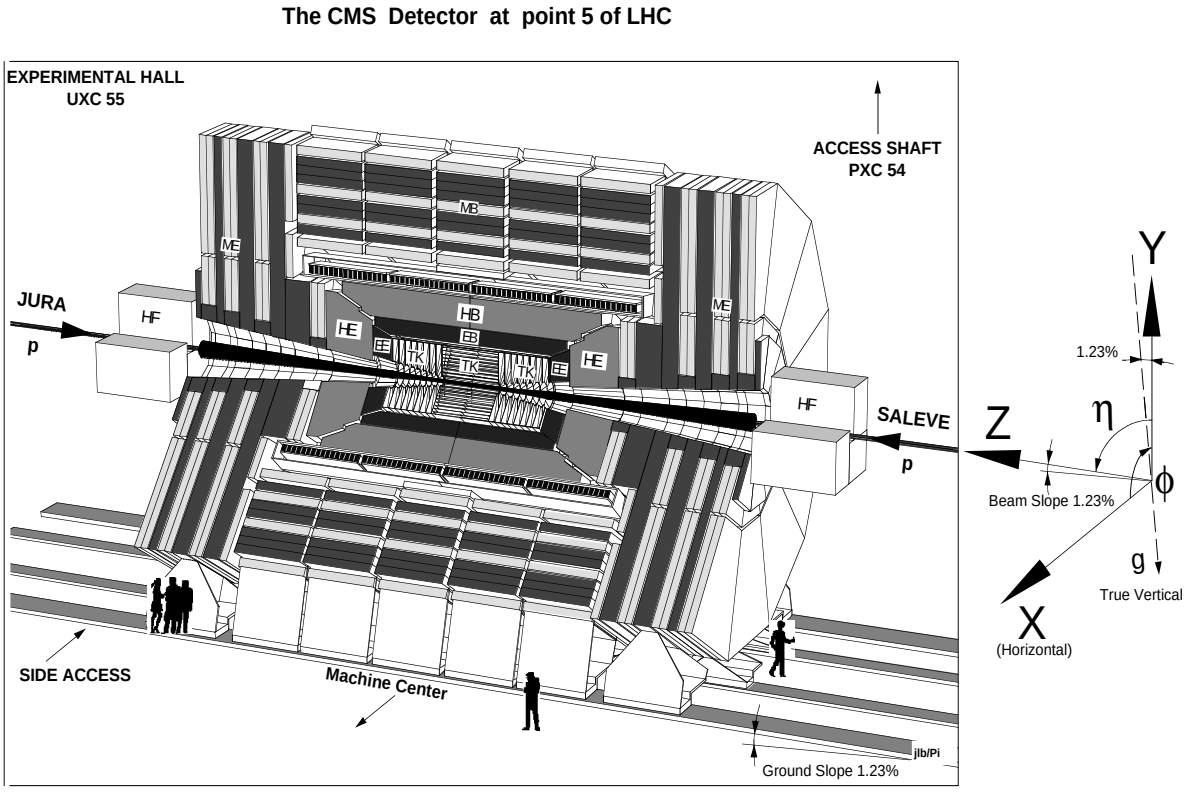

Figure 14: The CMS detector

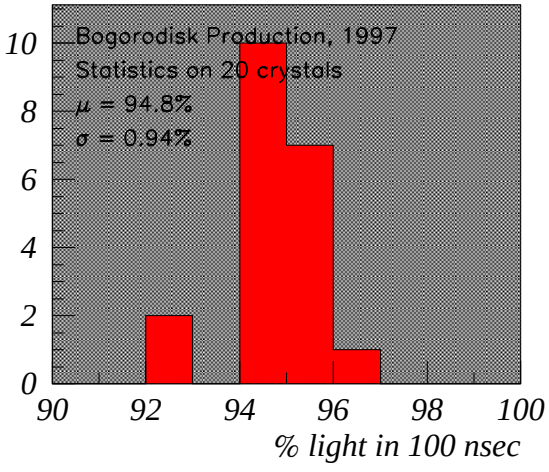

Figure 15: Percentage of light in 100nsec compared to 1μsec

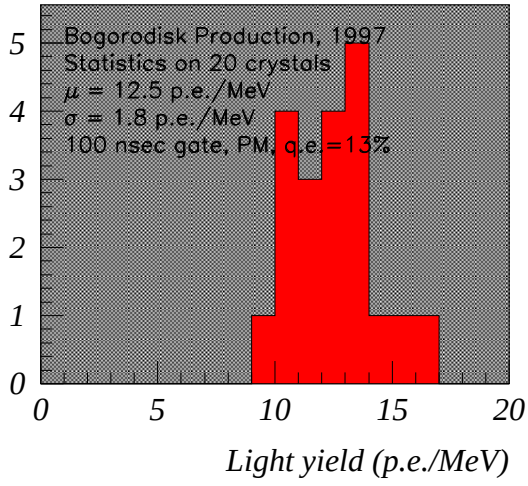

Figure 16: Light yield 2.5cm from the PM

measured with a PM tube which covers the whole of the rear surface of a crystal is equivalent to about 2.5 p.e./MeV into a 5x5mm^2 APD and about 5 p.e./MeV into a pair of APDs - as planned for the final CMS barrel ECAL.

- **Wavelength of light emitted**. Peak for $PbWO_4$ is around 450nm.
  - UV light is difficult to detect with silicon devices
  - transmission of light through the crystal depends on wavelength

    Figure 17 shows the radioluminescence spectrum for $PbWO_4$ crystals, together with the transmission curve. It is apparent that the complete scintillation spectrum can be transmitted through $PbWO_4$. However, impurities and non-uniformities in the crystals may result in absorption centres which will reduce this transmission, as described in the next section.

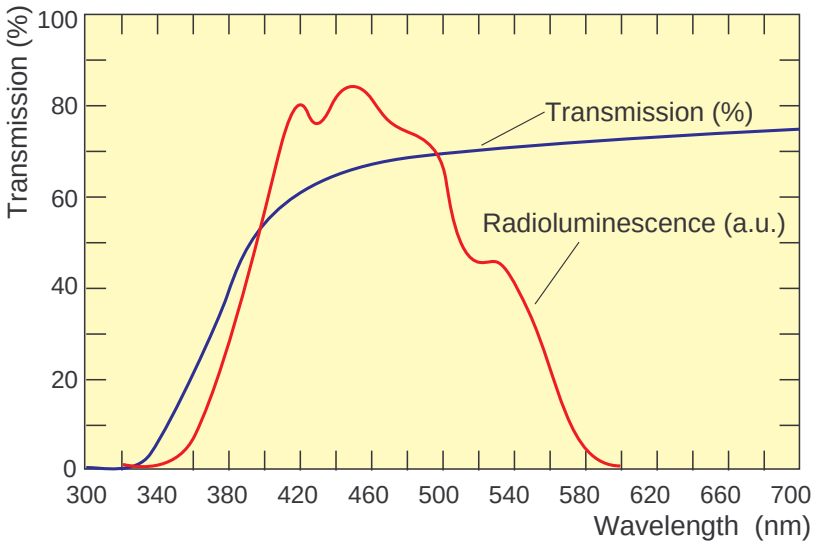

Figure 17: Radioluminescence and transmission spectra for $PbWO_4$ crystals

- **Radiation hard** - to neutrons, photons and charged particles see section 4.3
- **Substantial production capacity already exists**
  - Bogoroditsk - Russia
  - Shanghai Institute of Ceramics (SIC) - China
  - Kharkov - Ukraine
  - Crytur - Czech Republik
  - Carat - Ukraine

  During the production period (5 years) we expect to be able to make around 1500 crystals per month. The total number of crystals will be around 120000.

4.2 Optical Characteristics of the $PbWO_4$ Crystals

Figure 18 shows a schematic representation of a $PbWO_4$ crystal of the approximate dimensions to be used in the CMS barrel ECAL. The crystals are tapered such that they present a constant solid angle to particles coming from the interaction point.

In CMS the particles will be incident longitudinally (from the 'left' in the diagram) and this is also the standard way of testing the crystals in a testbeam. However, for some studies, such as measuring the transverse transmission or longitudinal uniformity the light or particles may be incident transversely, as shown.

Transmission and absorption

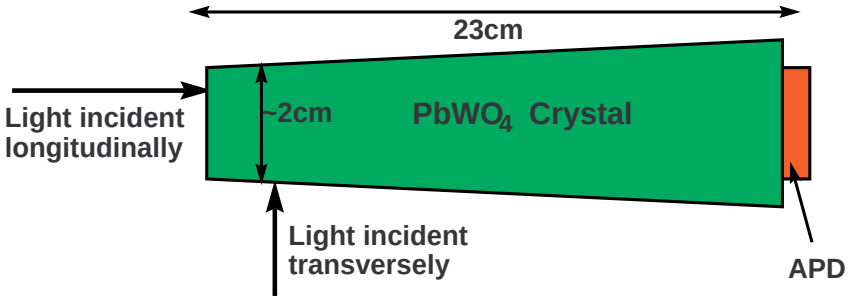

Figure 18: Schematic representation of a $PbWO_4$ crystal, showing the approximate dimensions to be used in CMS, the position of the APD and the directions of incidence of light and/or particles for various tests

Undoped crystals have difficulty transmitting light below 450nm, resulting in a loss of scintillation light. If the crystals are doped with an element such as niobium, lanthanum or lutetium then some absorption bands are removed, increasing the transmission at low wavelengths. Figure 19 shows transmission curves for undoped and doped crystals.

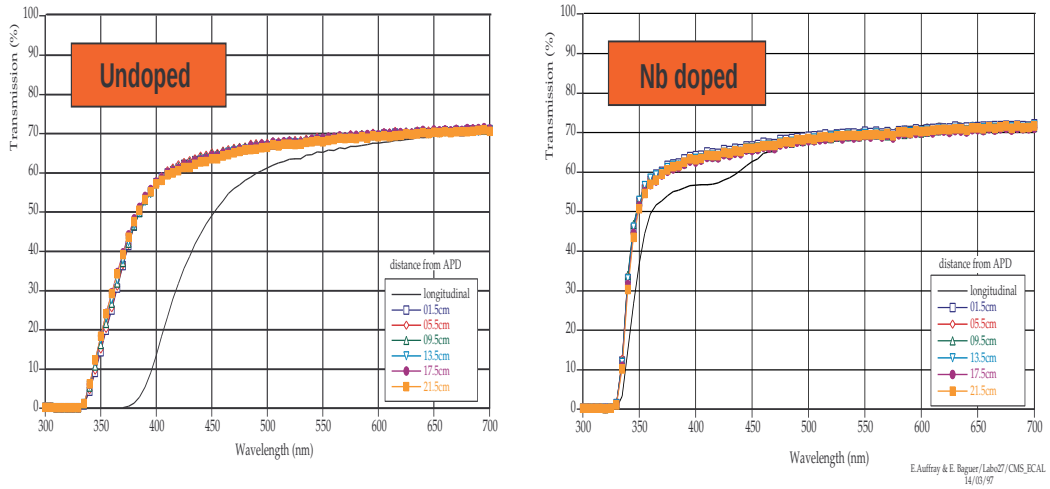

Figure 19: Transmission curves for undoped and niobium-doped crystals. The solid line shows the longitudinal transmission whilst the data points are transverse transmission measured at various points along the crystal.

The transmission edge for the niobium-doped crystals is much steeper, and the longitudinal transmission (light passes through 23cm of crystal) is virtually the same as the transverse transmission in this case.

These dopants are particularly important for the control of induced absorption (after irradiation), as demonstrated in figure 20 which shows the induced absorption as a function of wavelength for four full-size Russian crystals. The doped crystals are between a factor of 2 and 5 better (longer absorption length) than the undoped crystal.

Longitudinal Uniformity

The tapered shape of the crystals has a focussing effect on any light inside a crystal: light produced at the front of the crystal (farthest from the photodetector) is focussed more, and thus has more chance of being detected by the photodetector, than light produced towards the back of the crystal. However, if the absorption length of the crystal is relatively short, light produced at the front of the crystal has more chance of being absorbed than that produced at the back. The light collection efficiency is thus a function of position along the crystal, as illustrated in figure 21. The shape of the longitudinal light collection curve can contribute to the constant term.

The ideal shape is shown in figure 22.

The most important region is around the shower maximum. This region should have a flat response. It is useful for the curve to show an increase towards the back of the crystal such that late developing showers are enhanced - this reduces low energy tails.

Recent crystals have shown a marked increase in their absorption lengths, resulting in the light collection curves

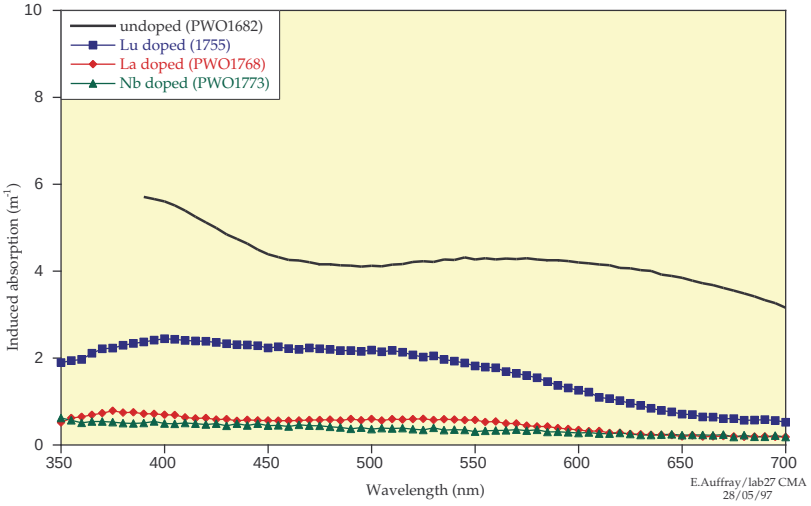

Figure 20: Induced absorption curves for 4 full-size Russian crystals. The longer the induced absorption length (i.e. lower on the vertical scale) the more 'transparent' the crystal.

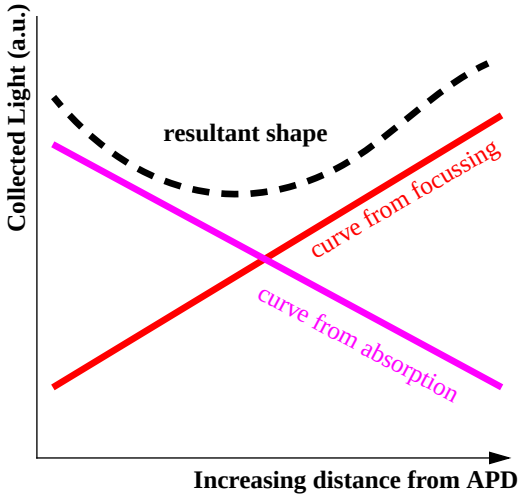

Figure 21: The longitudinal light collection curve - produced from the competing effects of focussing and absorption

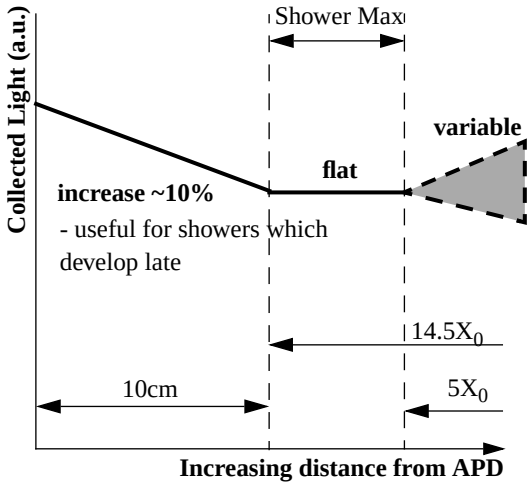

Figure 22: The ideal longitudinal light collection curve

being dominated by the focussing effect. This is far from the ideal case as the light collection decreases towards the back of the crystal. There is thus a need for crystal 'uniformization': systematic depolishing of parts of the crystal can change the light collection curve to be closer to the ideal case, thus reducing the contribution to the constant term. Figures 23 and 24 show the measured light collection curves for a single crystal before and after uniformization at CERN.

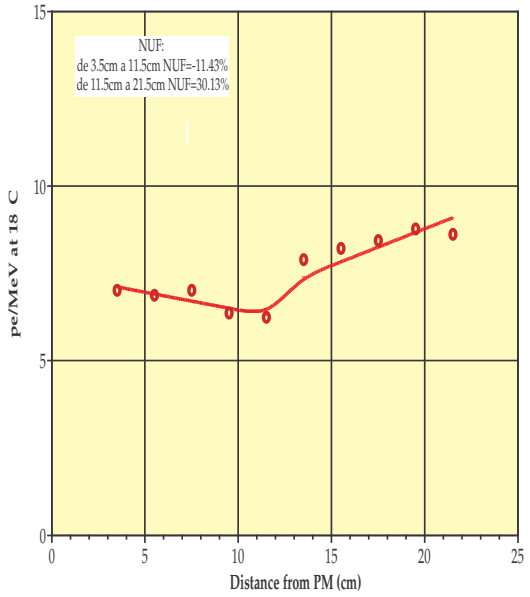

Figure 23: Light collection as a function of distance from the photodetector for a crystal before uniformization

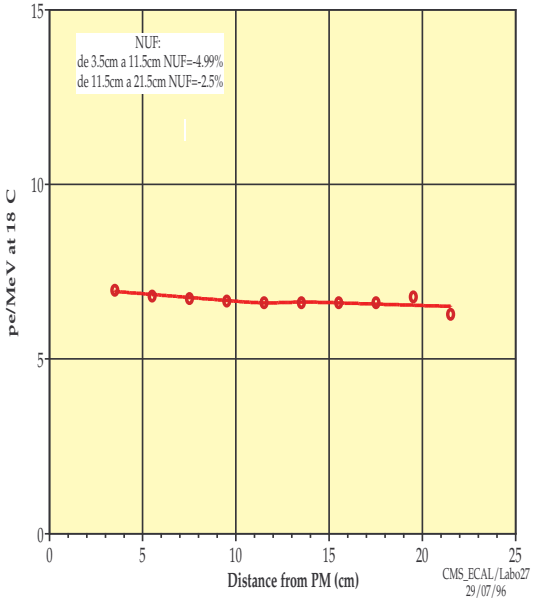

Figure 24: The corresponding light collection curve for the same crystal after uniformization

4.3 Radiation Tolerance

As mentioned previously, the radiation environment in CMS is extremely challenging. Lead tungstate crystals have been shown to be radiation hard to high (Mrads) levels, due to the fact that the scintillation mechanism is intrinsically radiation hard. However, some damage has been seen at surprisingly low levels in test beam experiments (few hundred rads, after which it saturates). The effect of radiation damage is to induce colour centres which reduce the transmission, and thus the amount of collected light; the scintillation mechanism remains unaffected. Recent progress has been made with doping and also with the crystal stoechiometry (the ratio between the two principle raw materials - lead oxide and tungsten trioxide). Figure 25 shows the induced absorption at 500nm after 50krad as a function of the stoechiometry. It is clear that there are minima in the induced absorption for certain mixtures.

Figure 26 then shows some recent results of low-dose radiation damage on various types of crystal. The light yield of each crystal is also given. The worst crystal is the one with non-optimized stoechiometry and also no doping. Optimizing the stoechiometry increases the radiation hardness and also increases the light yield. Doping with different elements then increases the radiation hardness further, whilst at the same time increasing the light yield.

To summarize, recent progress has shown that optimizing both the doping and stoechiometry not only increases the radiation tolerance but also the light yield of the crystals.

However, even with the best crystals there is still some small amount of low-level radiation damage. This necessitates an accurate in-situ monitoring system using either LED or laser light. This monitoring system can then be used to 'follow' the radiation damage (and recovery) to enable a correction to be applied to the measured energy deposits. Figure 27 shows the correspondance between signals due to an LED calibration pulse and to signals from electrons during test beam irradiation to 650 rads. The inset histogram is of the vertical distances of the points from the straight line fit, the gradient of which is used to perform the correction to the data. The width of the distribution of this inset histogram essentially gives the calibration error introduced by the use of the LED system, which should be kept to a small (less than 0.5%) level.

Figure 28 shows the energy spectrum measured by a 3x3 array of crystals due to 120 GeV electrons before and

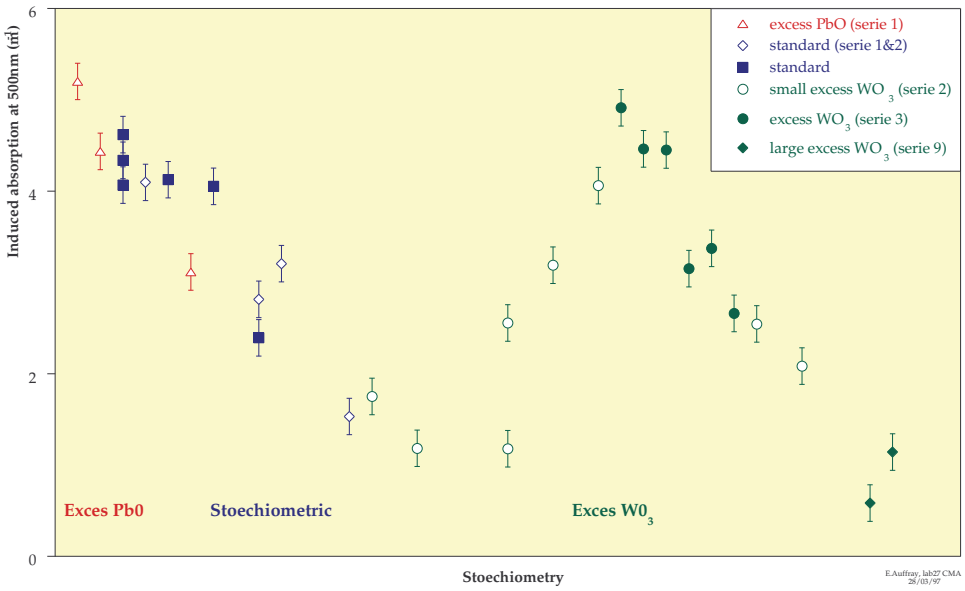

Figure 25: The variation of induced absorption length with stoechiometry for 29 full size Russian $PbWO_4$ crystals

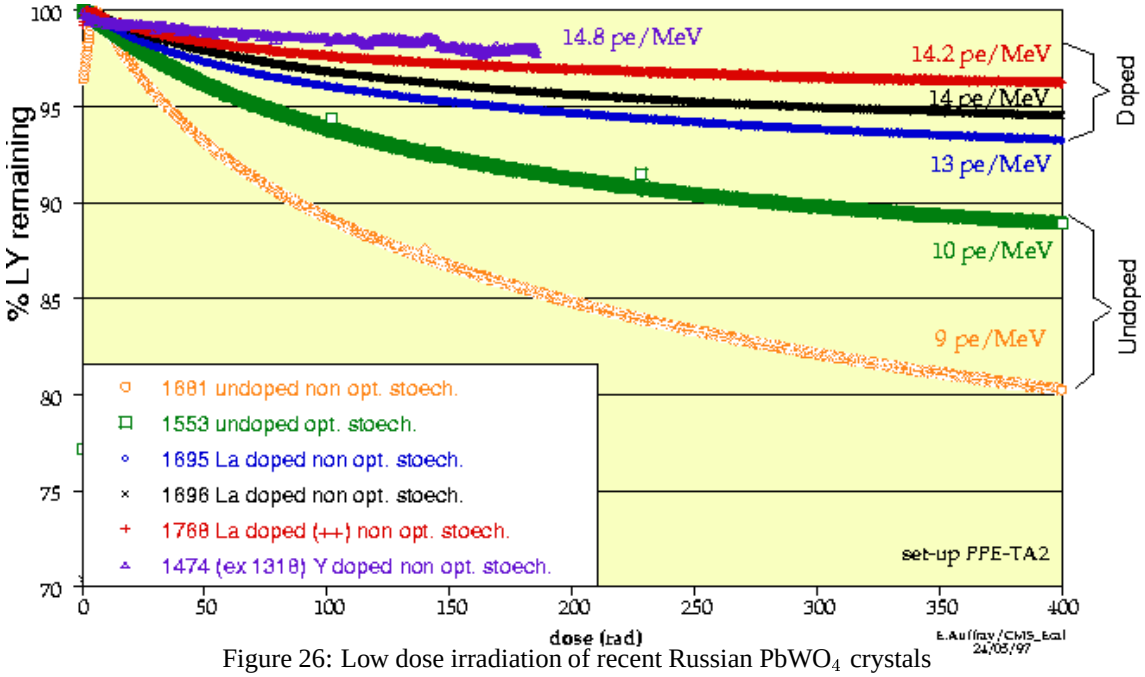

Figure 26: Low dose irradiation of recent Russian $PbWO_4$ crystals

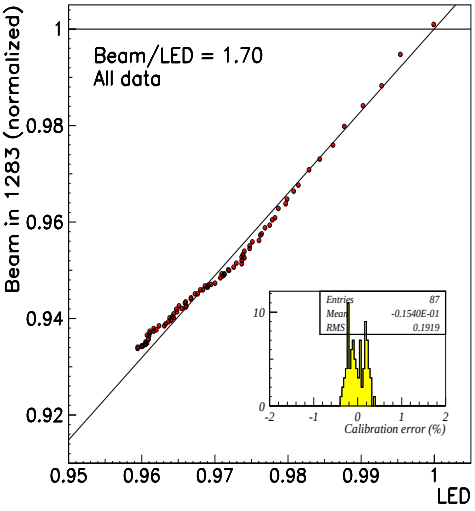

Figure 27: Correspondance between LED and beam signals during testbeam irradiation to 650 rads

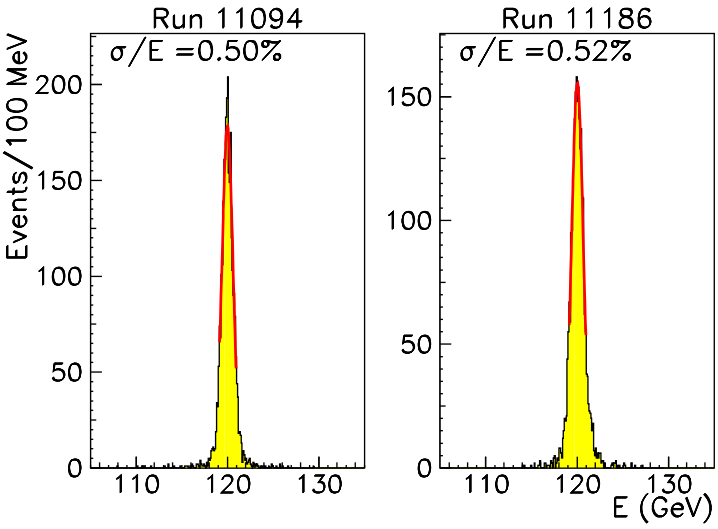

Figure 28: Energy spectra for 120 GeV e^- before (left) and after (right) irradiation to 650 rads

after irradiation to 650 rads. The data taken during and after irradiation have been corrected using the LED signal. The change in the measured energy resolution is within the experimental uncertainty which suggests that the scintillation mechanism has not been damaged. See [8] for more details.

4.4 ECAL Mechanical Structure

The CMS ECAL will contain approximately 120000 units; each unit consists of a lead tungstate crystal, readout device (see section 5) and associated readout electronics and optical/electronic calibration systems. In the ECAL barrel an array of 6 x 2 crystals is assembled inside a hollow 'alveolar' submodule. The alveolar is constructed from a low density two-layer composite material. The first layer (closest to the crystals) is a 25 μm aluminium foil which acts as a reflector for the light produced in the crystal and also aids mechanical rigidity. The second layer is a glass fibre epoxy resin 75μm thick. Although the walls of the alveolar are very thin - 100μm - the composite structure is extremely strong and enables a small inter-crystal gap of 0.4mm to be achieved within a submodule (including tolerances). The gap between crystals in adjacent submodules is a maximum of 0.6mm. Figure 29 shows the mechanical pieces which form a submodule. The alveolar unit is 'closed' by a foam bottom plate, into which fibres for the optical calibration system are mounted, and an aluminium top plate. Plastic cylinders inside the aluminium top plate freeze the crystal positions and allow accurate placement of the APDs.

Figure 30 shows a detailed view of the back of the crystals showing the placement of the APDs together with the supporting 'capsule' and very-front-end readout electronics.

A group of 12x4 submodules is assembled into a 'supermodule' as shown in figure 31 which provides further mechanical rigidity and includes support and cooling structures. Each supermodule weighs about 600kg. There are 8 supermodules in η and 18 in ϕ. The submodules inside the supermodule are angled by 3° such that the crystals do not point to the interaction vertex, reducing the effect of gaps between crystals.

The endcap ECAL has a different overall structure to the barrel. The crystals have square front and rear faces which are slightly larger than in the barrel, but are tapered in a different way to the barrel, as shown in figure 32 in order to achieve off-pointing in two dimensions. The presence of the endcap preshower, containing approximately 3 X_0 of absorber, allows the crystals to be shorter (by 1cm) than in the barrel. Arrays of 6x6 crystals are placed inside alveolar structures similar to those used in the barrel to form identical 'supercrystals' and these supercrystals are arranged in an 'x-y' grid to cover the majority of the endcap fiducial area - see figure 33. The remaining area, on the outer and inner radii, is covered by dedicated modules.

The overall layout of the CMS ECAL is shown in figure 34 including the endcap preshower.

The barrel ECAL extends up to η = 1.479, whilst the endcap covers the region $1.479 < \eta < 2.61$. Pileup effects and radiation damage limit the performance of the calorimeter at very high η so the 'precision coverage' is defined as the region $|\eta| < 2.5$ (excluding the barrel/endcap interface region).

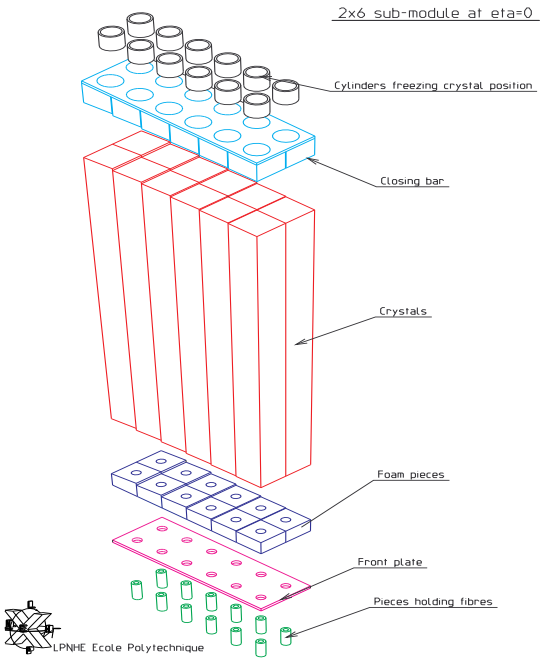

Figure 29: The mechanical structure of a barrel ECAL submodule

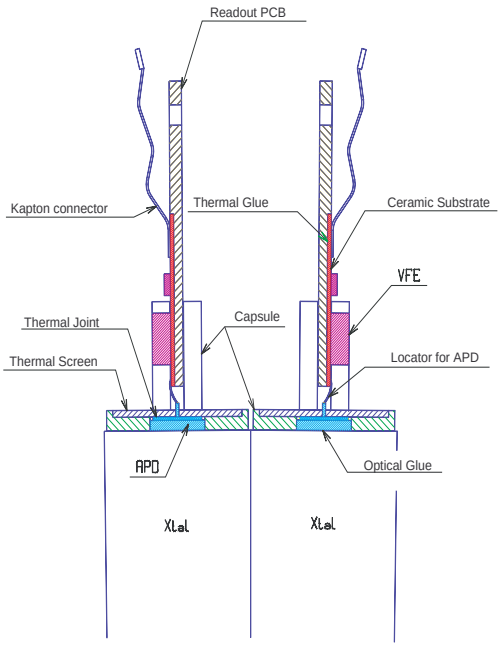

Figure 30: A detailed view of the placement of the APDs on the back of the crystals

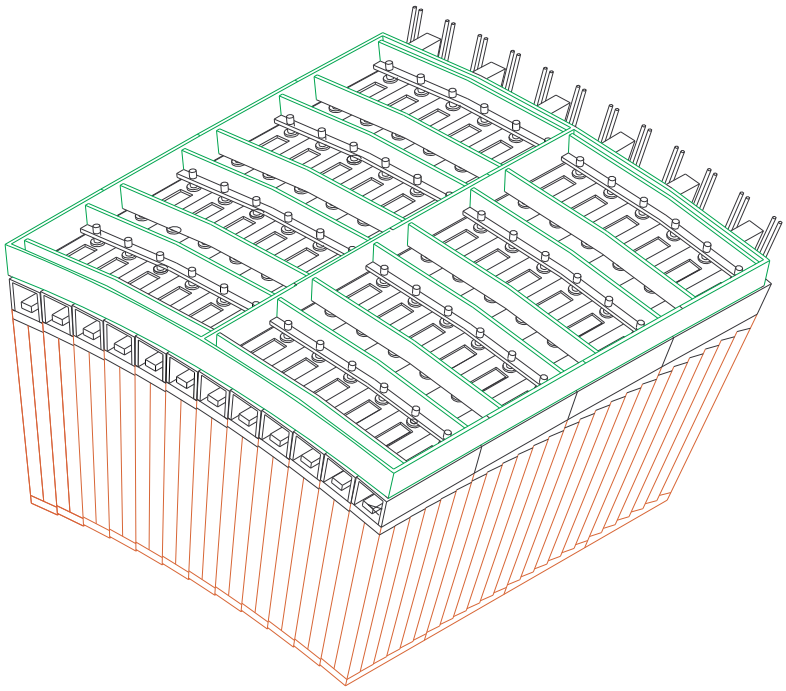

Figure 31: The mechanical structure of a barrel supermodule

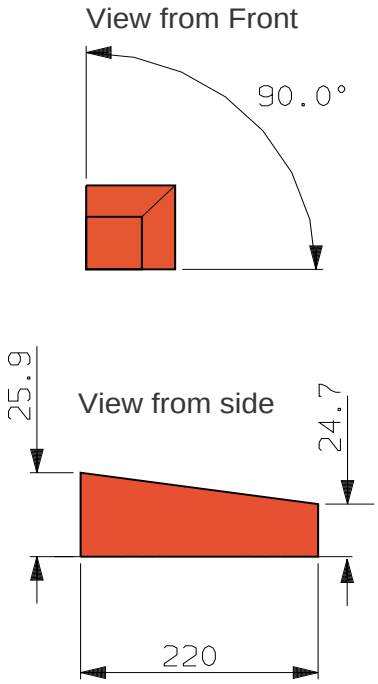

Figure 32: The dimensions of an endcap crystal

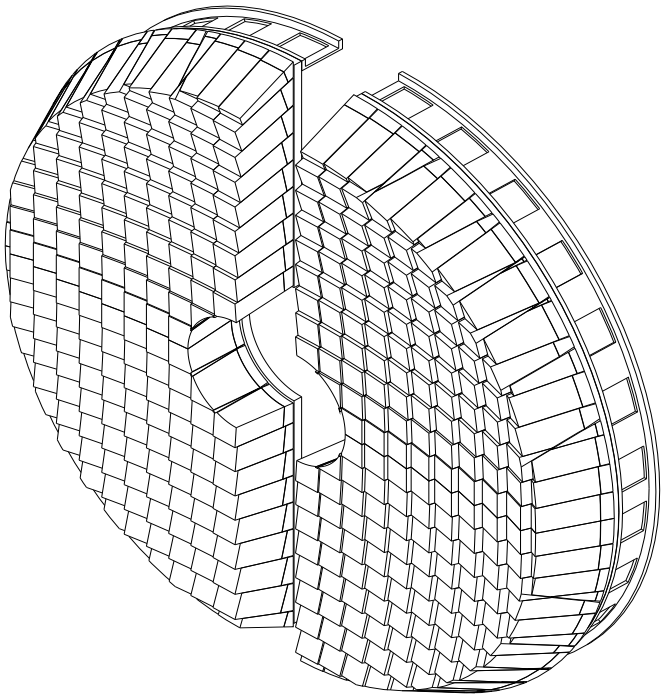

Figure 33: The endcap supercrystal layout

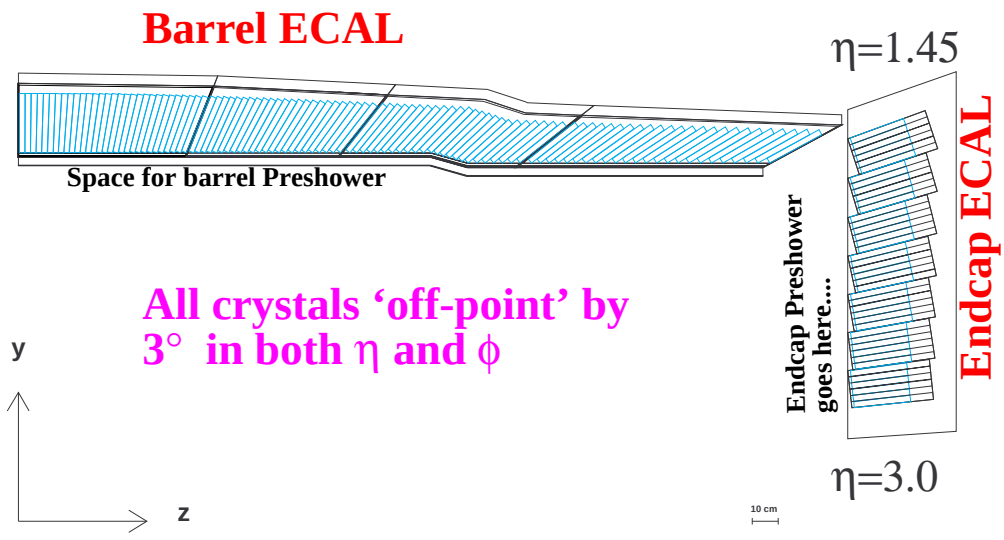

Figure 34: The overall layout of the CMS ECAL. The 'step' in basket 3 of the barrel ECAL enables the barrel preshower to be present if necessary at high luminosity. It should be noted that this design is now obselete: the step is no longer present - it is envisaged that if the barrel preshower is necessary, the final layer of MSGCs in the CMS tracker will be removed to make space (see section 8).

5 Photodetectors and Electronics

The relatively low light output of the lead tungstate crystals imposes strict requirements on the type of photodetector used: it must have internal amplification and low noise. Further constraints are the high magnetic field (4T), the compact structure of CMS and the severe radiation environment - particularly in the endcaps. This last constraint has the effect that the photodetectors used in the barrel are not the same as those used in the endcaps.

5.1 Avalanche Photodiodes - APDs

The requirements for a compact amplifying photodetector which is able to operate in a high magnetic field are satisfied by a breed of silicon detectors called avalanche photodiodes (APDs). These devices are similar in principle to conventional silicon photodiodes, but they contain a multiplication region which can give a gain of up to a few hundred, depending on how they are constucted. A schematic section through such a device is given in figure 35.

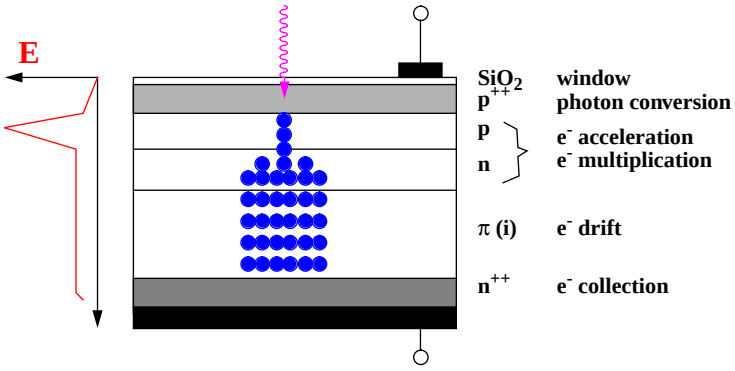

Figure 35: Schematic cross-section of an APD

Essentially, an incident photon is converted to an electron-hole pair in the p^{++} layer, the electron is accelerated (causing multiplication) in the high field p and n regions, and then the 'cloud' drifts in a region of intrinsic silicon and is finally collected.

APDs have some important advantages:

- internal gain of between 50 and 200 - operate at a gain of 50
- low capacitance (due to drift region)
- ability to operate in a high magnetic field
- compact - few tens of microns thick
- sufficiently radiation hard to withstand the neutron flux in the barrel

However, it is relatively difficult to manufacture an APD with a large area: the maximum size of suitable APDs available at present is about 5x5mm^2. This is a small fraction of the rear surface of the crystal, so it is planned to use two APDs per crystal in CMS such that the performance of the ECAL is not limited by the photostatistics contribution to the stochastic term. The gain of the devices is sensitive to temperature - approximately 2% per °C. The fluctuations in the leakage current increase with radiation damage such that APDs are unsuitable for use in the endcaps.

One additional disadvantage of APDs is their potential sensitivity to ionizing particles. A minimum ionizing particle ('mip') traversing a conventional PIN silicon detector will deposit, on average, about 100 keV in 300 μm of silicon. Although APDs are very thin, the amplification region can result in an extremely large signal being produced from a single incident mip, as depicted in figure 36.

An effective thickness 'ϵ' can be defined as follows:

$$n_e = 100(L_\pi + \epsilon.M) \tag{8}$$

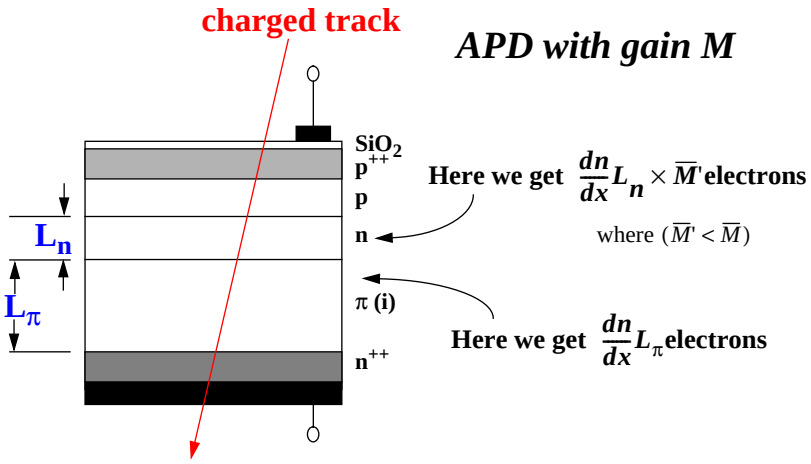

Figure 36: The sensitivity to ionizing radiation of an APD

The effective thickness is between about $5\mu m$ (Hamamatsu) and $12\mu m$ (EG&G) at a gain of 50. The signal from a mip traversing an APD is then approximately $40 \times \epsilon$ MeV.

Careful design and manufacture of the various silicon layers can limit this sensitivity (see section 7.3).

5.2 Vacuum Phototriodes

As mentioned previously the radiation environment in the endcaps in CMS preclude the use of APDs. Vacuum phototriodes ('VPTs') similar to those used by the OPAL experiment at LEP could be used, but need to be about 1/4 of the size. VPTs have lower gain than APDs but the signal-to-noise requirements in the endcaps are much lower so this is not a problem. The principles of operation of VPTs are similar to conventional photomultiplier tubes. Electrons liberated by a photon incident on a semi-transparent photocathode are accelerated towards an anode mesh. The electrons can pass through the mesh towards a dynode, where multiplication occurs. The resulting electrons are attracted towards the anode, where they are 'detected'. A schematic diagram of a VPT is shown in figure 37 below. This configuration of electrodes results in the possibility of operation in a high magnetic field, as also demonstrated by the plot in figure 37 which shows the relative output of two phototriodes and one type of phototetrode as a function of magnetic field strength.

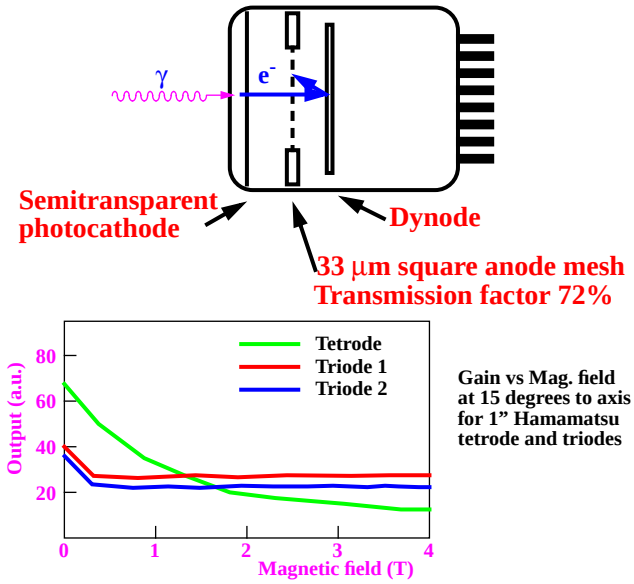

Figure 37: Schematic diagram of a VPT together with a diagram showing their gain response in a magnetic field

These devices are currently under study in Japan, Russia and the UK.

5.3 Readout Chain

The requirement for the readout chain is that signals must be output at 40 MHz *without degrading the energy resolution*. This means that a large dynamic range must be allowed (25 MeV $\longrightarrow$ 2 TeV) and that the digitization precision must be better than 0.1%. A schematic representation of the readout chain is given in figure 38.

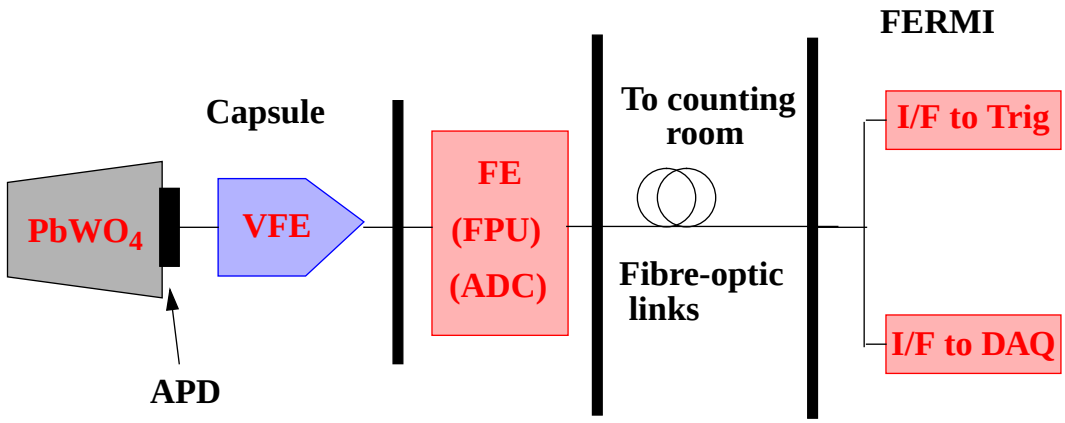

Figure 38: The CMS ECAL readout chain

The readout electronics consist of three principle parts as described briefly below.

VFE - Very Front End This shapes and amplifies the analogue signal from APD or VPT. It will be based on either a charge-sensitive or transimpedence low-noise amplifier with the required large dynamic range.

FE - Front End This includes a floating-point unit (FPU) for pedestal adjustment and zero suppression. An 11-bit 80 MHz ADC will be incorporated for compression and digitization. These compressed digital signals will then be transmitted optically to the counting room.

FERMI This is a multichannel DAQ and signal processing module. Digital data are sent both to the trigger and to the central DAQ system.

6 The Preshowers

The basic structure of the preshower devices used in CMS is a layer of a dense 'absorber' material followed by a silicon microstrip detector plane. Photons incident on the absorber will start to shower; electrons/positrons generated in the shower will give rise to signals in the silicon detector; these signals enable the position of incidence of the initial photon to be measured. The energy deposited in the absorber must, however, be measured in some way. This means that the signal from the silicon strips must also be used to apply a correction to the energy measured by the crystals. The correction is never perfect, due to fluctuations in the energy deposited in the absorber, so the energy resolution of the ECAL is degraded slightly.

The CMS detector includes two preshower detectors: one in the barrel and one in the endcaps. They are similar in design but have very different functions:

Barrel Preshower To measure, in conjunction with the crystals, the angle of incidence of the incoming photons (see section 7.6).

Endcap Preshower To distinguish energy deposits in the ECAL caused by single photons and photons from the decay of neutral pions.

In addition to these specialised functions, the preshowers also aid in electron/$\pi^{\pm}$ separation and, due to the absorber material in front of the crystals, reduce rear leakage from high energy showers.

Figure 39 shows a cross-section of the endcap preshower at $\eta = 1.7$ with a single incident 20 GeV E_t photon. Only charged tracks are shown. The endcap preshower device comprises two absorber layers, of approximately 2 X_0 and 1X_0 thickness respectively, each followed by a plane of silicon detectors. The shower can be seen to develop and the charged tracks are incident on the silicon detectors. Each silicon detector contains 32 strips, and the signal in each strip of a single detector in each of the two planes is also shown.

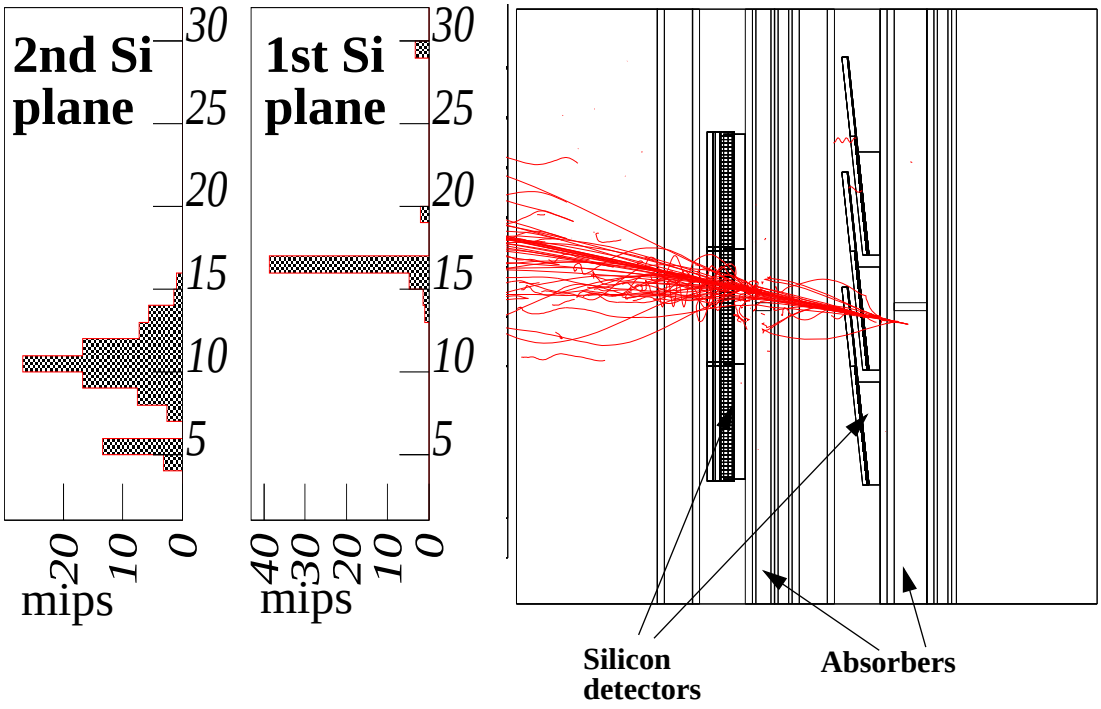

Figure 39: Cross-section of the endcap preshower at $\eta = 1.7$ showing a single incident photon. The signals in each of the two (orthogonal) detector layers is also shown.

The following sections describe the basic functions of the preshowers and present some results obtained from experiment and simulation.

6.1 Necessity for Preshowers

6.1.1 Barrel Preshower

The principle reason for including a barrel preshower is to measure the angle of incidence of photons. It was mentioned previously (see eqn. 5) that the mass resolution of an intermediate mass Higgs decaying to two photons depends upon both the energy resolution and the accuracy of the measurement of the angle between the two photons. This angle requires a knowledge of the decay point of the Higgs, which due to the short lifetime is essentially the same as the interaction vertex. The bunches of protons in the LHC will be very localized in the transverse plane (r.m.s. spread of about 15 μm) but the spread longitudinally (along the beam direction) has an r.m.s. width of about 5.3cm. If this vertex position is not known, and we simply use the centre of CMS as an estimate of the vertex position, then an additional contribution to the mass resolution of about 1.5 GeV will result.

In the low luminosity phase of the LHC there are, on average, one or two interactions per bunch crossing. Consequently, charged tracks which also come from the interaction vertex can be used to measure the vertex position along the Z axis. In high luminosity running there are on average 17 interactions per bunch crossing. Finding the correct primary vertex (associated to the Higgs) is thus more difficult. It is thought that some high p_t charged tracks will be associated with the Higgs production, and if this is the case then these may be used to locate the vertex. However, if this is not the case then the vertex must be located by the use of a barrel preshower: a photon position measurement in the preshower, together with a measurement in the crystals, will allow the photon direction, and thus the primary vertex, to be measured. Figure 40 shows the contribution to the Higgs mass resolution which would arise as a function of the coverage in η of a barrel preshower, assuming that the vertex could not be located in any other way. The angular resolution of the preshower-crystal system is assumed to scale as either 40 or 50 mrad / $\sqrt{E}$.

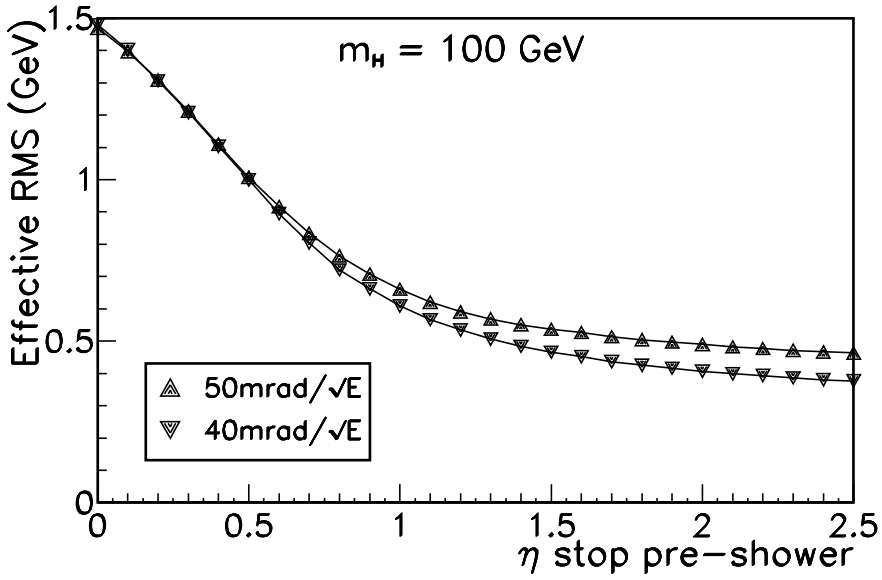

Figure 40: Contribution to the Higgs mass resolution at high luminosity as a function of the η coverage of the barrel preshower.

It is apparent that there is no appreciable advantage in having the barrel preshower cover an area greater than about $|\eta| \leq 1$. At present it is unclear as to the necessity of the barrel preshower - it is retained as an option for high luminosity running.

6.1.2 Endcap Preshower

One of the major reducible backgrounds to the H$\longrightarrow \gamma\gamma$ channel is from neutral pions in jets which fake single isolated photons. In the barrel the mean separation between the two photons from the decay of a π^0 is around 1cm at the radius of the ECAL. Consequently the crystals can be used to distinguish between single incident photons and pairs of photons from π^0s to a great extent. However, in the endcaps the energy of the pions and photons is greater so the separation between the photons from π^0s is smaller, of the order of a few mm. A position-sensitive device with sufficient granularity placed upstream of the crystals can be used to identify and reject energy clusters from the photons from π^0s, as demonstrated in figure 41.

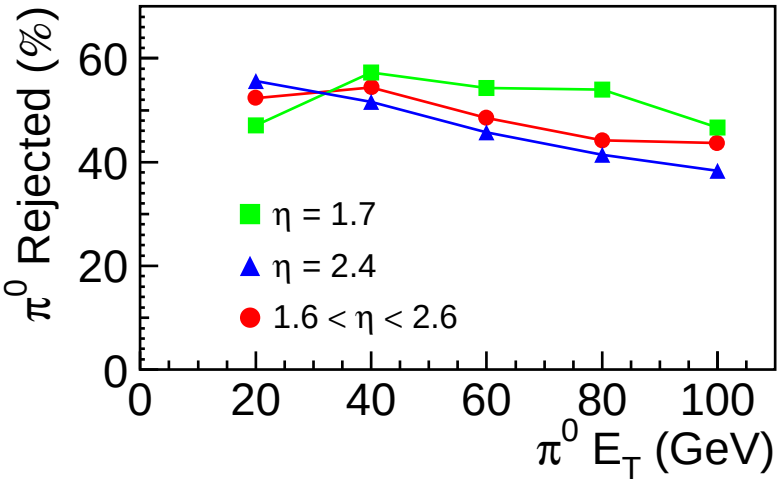

Figure 41: Neutral pion rejection in the endcaps of CMS using either crystals or a preshower, as a function of $\pi^0 E_t$. The efficiency for single photons has been set to 90%.

The π^0 rejection power of the endcap preshower is rather flat as a function of E_t, even at large values of η where the separation of the photons is of the order of 1mm. Above an E_t of about 30 GeV, the rejection power of the crystals alone in the endcap is around 20%. The algorithm used to reject photons from π^0s in the preshower is rather simple; a more sophisticated algorithm, perhaps employing a neural network, should improve the rejection power.

6.2 Detector Requirements

The structure of a preshower detector must be chosen carefully.

Absorber thickness The absorber must be thick enough (in terms of X_0) to initiate photon showers most of the time, but not too thick to excessively degrade the energy resolution. Figure 42 shows the effect that a preshower would have upon the energy resolution of an ECAL, as measured in a testbeam at CERN; the 'added term' should be added in quadrature to the energy resolution of the crystals alone. The preshower used comprised 2.5 X_0 of lead absorber followed by a single silicon detector plane - representative of the barrel preshower.

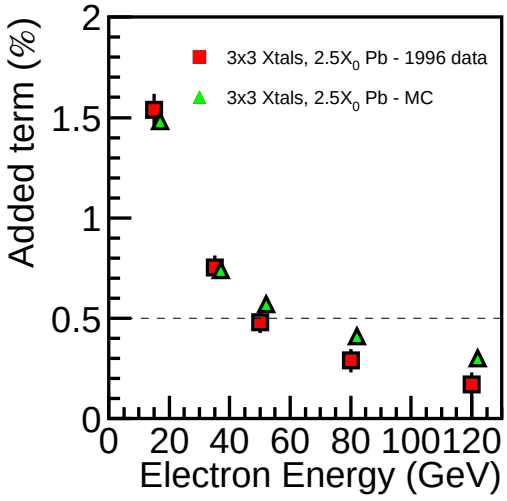

Figure 42: Preshower additional term as a function of electron energy for data and simulation.

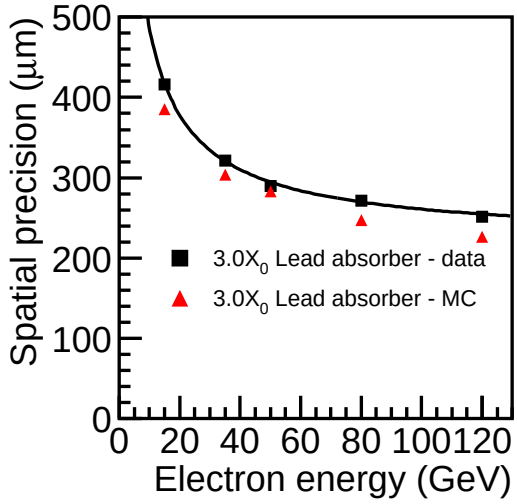

Figure 43: Preshower spatial precision as a function of incident electron energy when 3 radiation lengths of absorber are present

When a 5x5 array of crystals is used to measure the energy the preshower added term is much smaller: the showers initiated in the preshower absorber spread transversally, such that energy may be deposited outside of a 3x3 array.

Compactness The lateral containment of showers by the crystals is clearly a function of distance between the absorber and the crystals. This is particularly important in the barrel due to the unfavourable direction of the magnetic field. The preshower should thus be as compact and as close to the crystals as possible.

Strip Pitch The pitch of the microstrips in the silicon detectors does not have to be too fine as the requirements for position resolution are not too strict. In fact the strips are about 1.9mm x 60mm. The spatial precision obtained from these relatively wide strips is shown in figure 43.

The spatial precision, as measured with the silicon strips following 3 X_0 of absorber, may be approximated as:

$$\sigma Y(\mu m) = \frac{1370}{\sqrt{E}} \oplus 260 \tag{9}$$

6.3 Preshower Mechanical Construction

Figure 44 shows a detailed drawing of the endcap preshower mechanical structure. It essentially consists of two layers of lead absorber, each followed by a silicon detector array. The first absorber layer (actually an iron-lead-iron 'sandwich') is about 2 X_0 thick whilst the second is about 1 X_0 thick. The silicon detectors are about 6cm x 6cm and are supported on aluminium 'wedges' which allow detector overlap in one direction. The two detector layers have their silicon strips aligned in orthogonal directions. The cooling structures, and neutron absorber layers[4], are also shown. Particles are incident from the left.

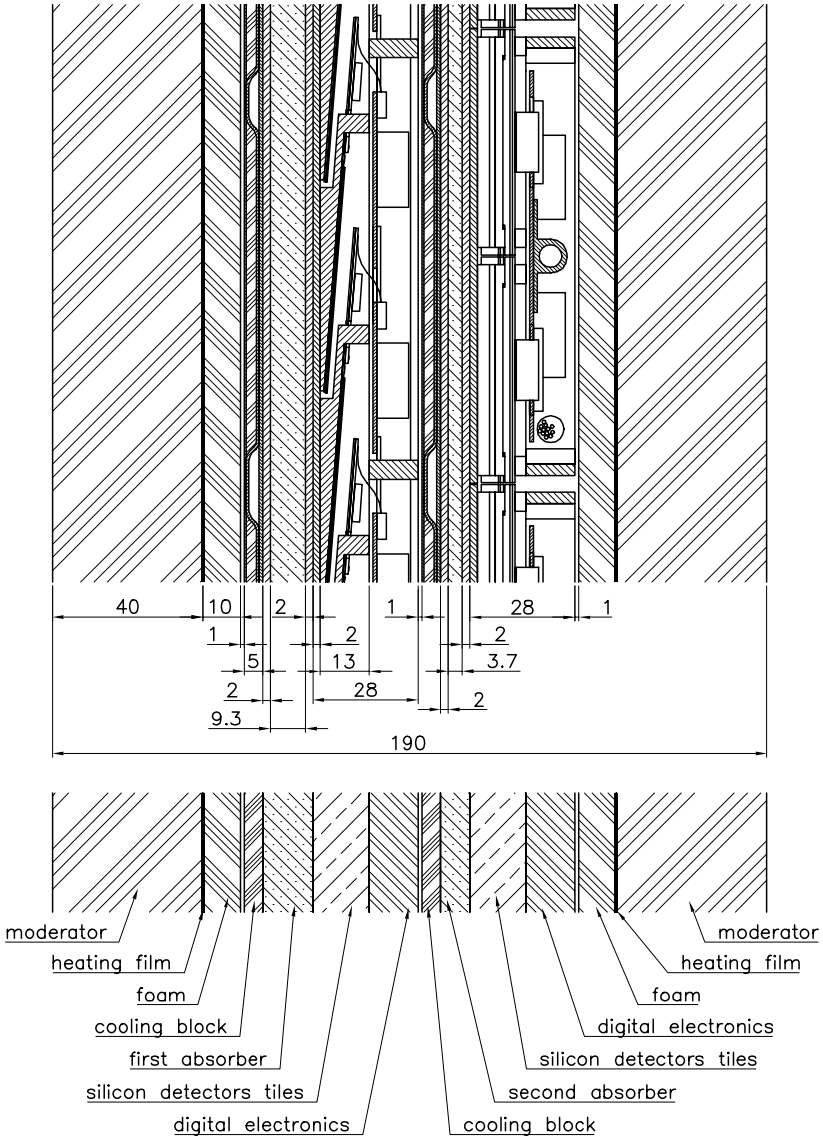

Figure 44: Endcap preshower cross-section: schematic view (bottom) and mechanical design (top). All dimensions are in millimetres.

The construction of the barrel preshower is similar, except that only one absorber layer (2.5 X_0) will be used. Figure 45 shows the positions of the endcap ('SE') and barrel ('SB') preshowers in CMS. The barrel preshower, covering the range $|\eta| < 1.1$, will not be included at the startup of CMS as its necessity depends upon the exact nature of both Higgs and minimum-bias events which will not be known until the LHC starts running. The endcap preshower, covering the range $1.479 < \eta < 2.61$, is a baseline item and will be present at the startup of CMS.

[4] Neutrons created by nuclear interations in the ECAL crystals can damage silicon detectors, both in the preshower and the tracker

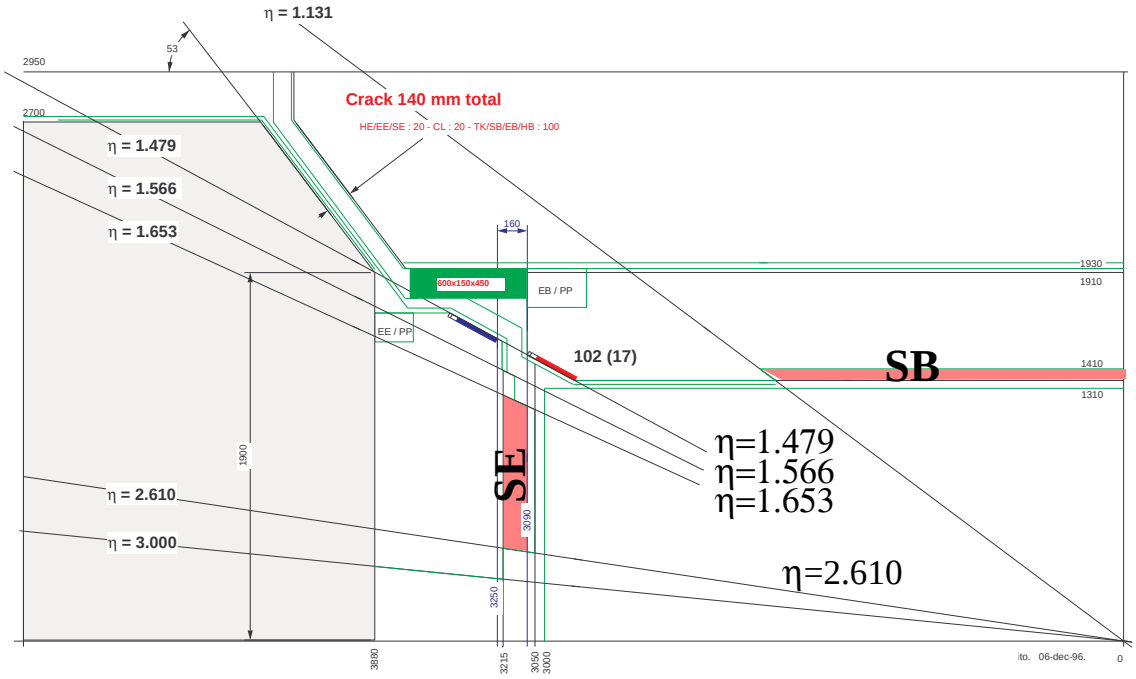

Figure 45: Approximate positions of the endcap and barrel preshowers in CMS

6.4 Preshower Electronics

6.4.1 Front-end

In contrast to most silicon detectors, particularly those used in tracking devices, the preshower detectors have to operate over a large dynamic range. This is due to the necessity of measuring a m.i.p. signal with an S/N ≈ 5 (for calibration) and measuring large signals (equivalent to a few hundred m.i.p.s) due to electron/photon showers with $\approx 5\%$ accuracy. To achieve these aims, a custom readout system designated 'PACE' (Preshower Analog CMS Electronics) has been designed at CERN and successfully tested. Each PACE chip will readout signals at 40 MHz from a single 32-channel silicon detector and store these signals for up to 4 μs. The charge deposited in the silicon due to the passage of a m.i.p. or shower is generally spread over 2 or 3 time samples so the dynamic range does not have to be prohibitively large - a dynamic range of 250 m.i.p.s is sufficient.

Figure 46 shows a block diagram of the PACE chip. Signals from the silicon are stored, after amplification, in the analog memory. If a first-level trigger is received the addresses of the corresponding memory cells are stored in the FIFO. The corresponding second-level trigger may not be received in 4 μsec so a 'skip controller' is used such that these memory cells are not overwritten. When the second-level trigger arrives, the addresses of the appropriate memory cells are retieved from the FIFO and the data are passed, via read amplifiers, to a multiplexer.

6.4.2 Readout Architecture

The multiplexed analog signals from the front-end are passed to ADC's and then into digital processing units which perform such tasks as pedestal subtraction, suppression of common-mode noise and data sparsification. Much of the electronics, including the optical links, were originally developed for the CMS tracker.

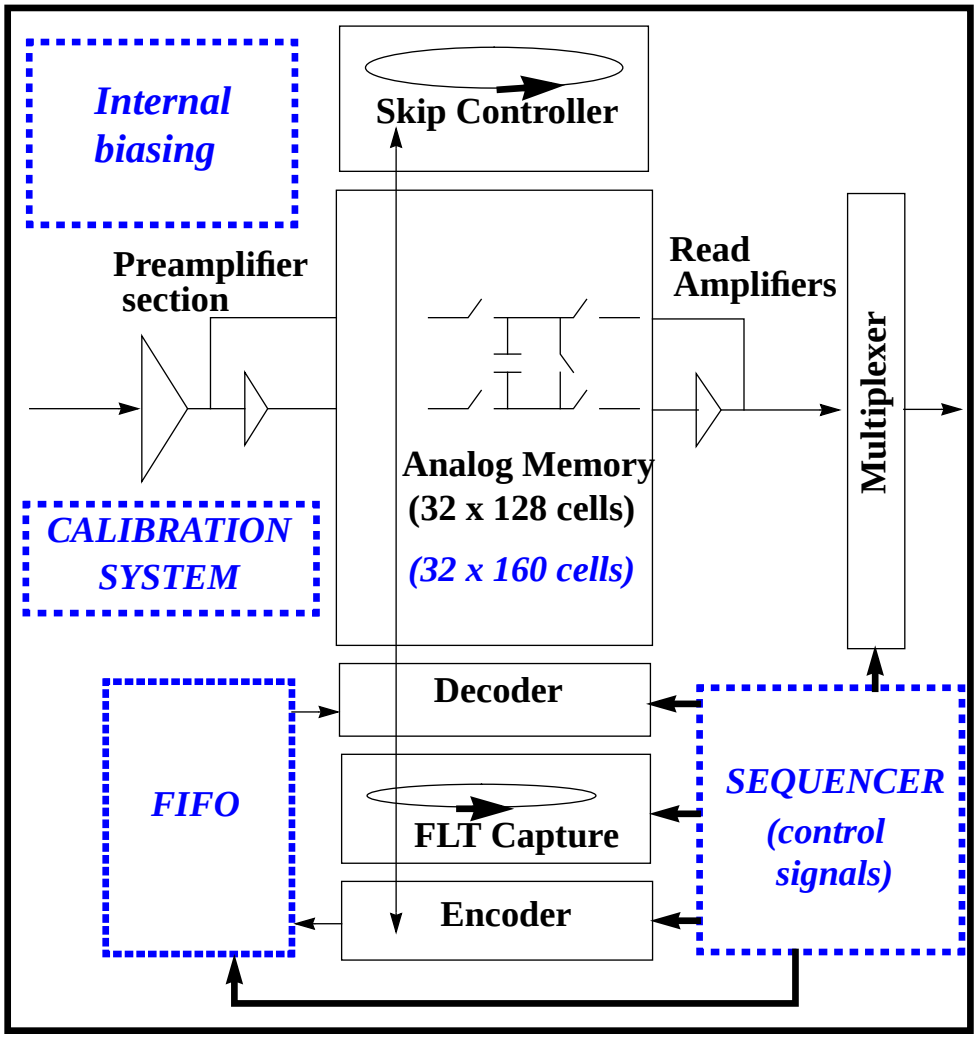

Figure 46: Block diagram showing the layout of the preshower front-end chip - PACE

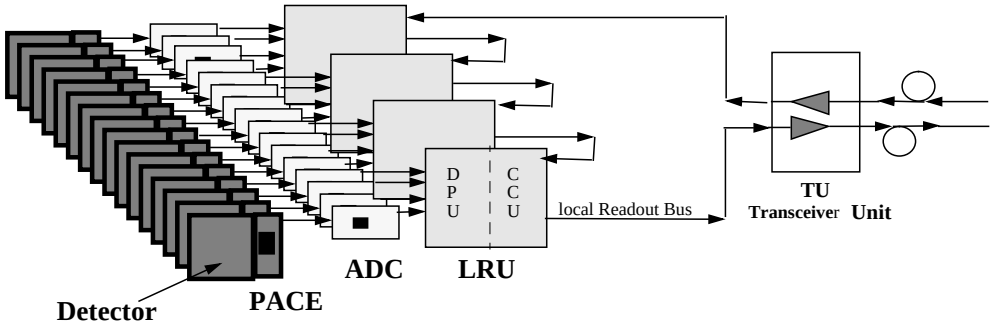

Figure 47: Preshower readout architecture

7 Testbeam Results

Many testbeam results, principally concerning energy resolution, have already been presented in this report. This section will show additional results on subjects such as temperature stability, position resolution of crystals and electron/charged-pion separation. The progress achieved with the APD nuclear counter effect is also shown.

7.1 Testbeam Setup

The principle aim of the ECAL beam tests is to measure the energy resolution of a crystal array as a function of energy. Arrays of up to 7×7 crystals have been examined but the system is capable of testing an array of up to 10×10. Copper 'crystals' are used to surround the real crystals providing temperature and mechanical stability. The array is arranged such that it is representative of the CMS ECAL at $\eta = 0$. As both the crystals and APDs are temperature sensitive the matrix is placed in a light-tight temperature stabilized containment box. This containment system is then placed on a moveable table, allowing rotation and translation with respect to the beam. The principle beam line used was 'H4' in CERN's North Area which provides electron, pion and muon beams with a small momentum spread. Most tests were performed with incident electrons, in the energy range 10 GeV to 150 GeV (selectable) with pions and muons being used for some specific tests. In addition, a prototype preshower system was occasionally attached to the containment box. Figure 48 shows a schematic view of the testbeam setup used in 1996 and 1997. Scintillators and wire chambers upstream of the crystal matrix provided triggering and position of incidence information.

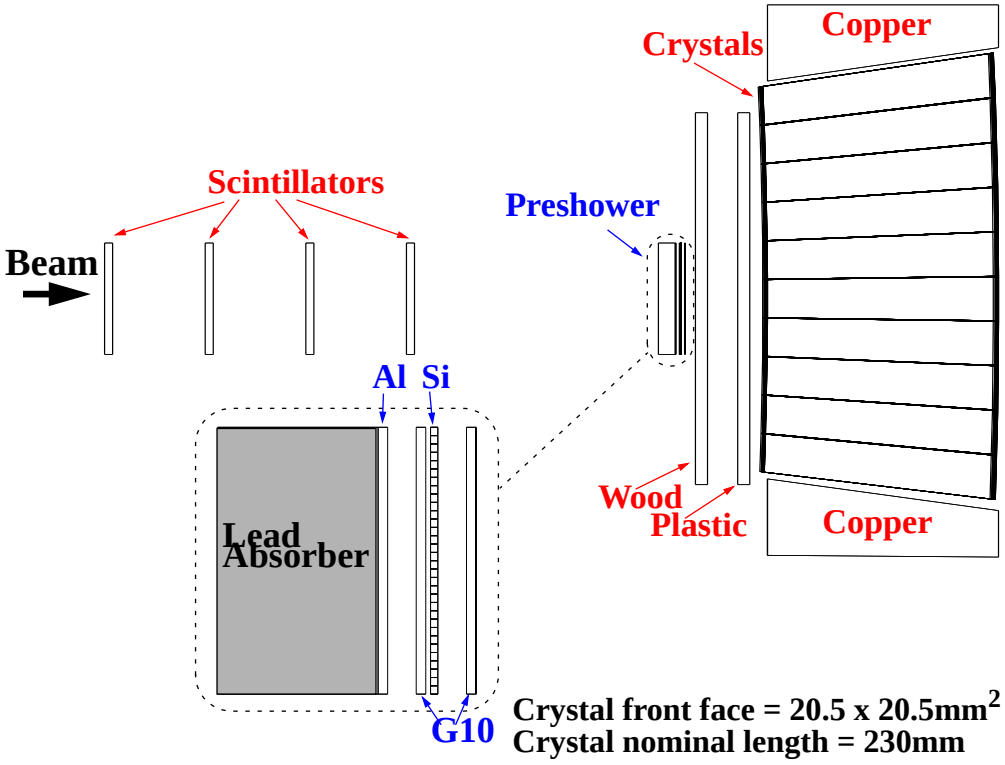

Figure 48: Schematic view of the testbeam setup

7.2 Temperature Stability

As mentioned previously, the crystals and APDs are sensitive to temperature variations. The temperature stability of the crystals is thus of utmost importance. In the testbeam the principle source of heat is from the preamplifiers attached directly to the APDs. A water cooling system has been employed to extremely good effect, as shown in figure 49 which illustarates the temperature measured at the back of one crystal over the course of 5 days. A regular cycle is apparent, due to residual day-night temperature variations. However, this fluctuation is of the order of $\pm 0.05^o$ which is sufficiently low that it has a negligible effect on the constant term.

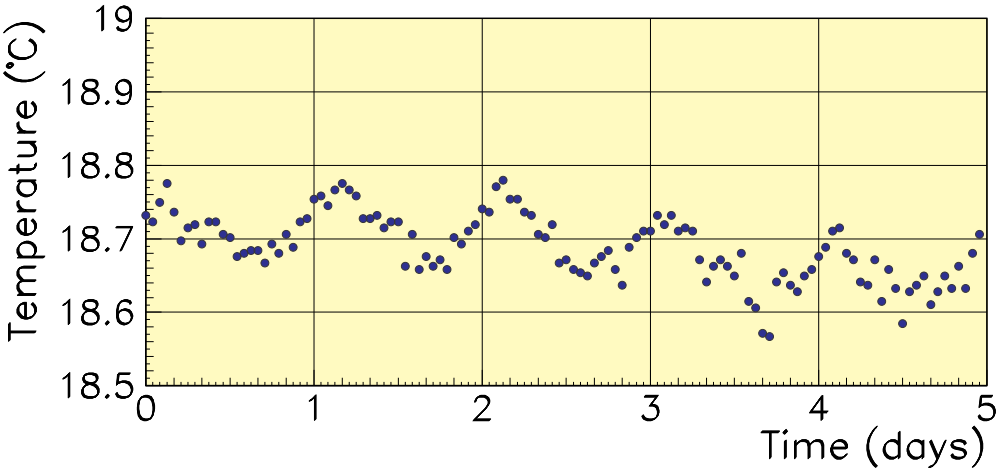

Figure 49: Temperature variation at the back of one crystal during a beam test

7.3 Nuclear Counter Effect

Ionizing particles traversing the APDs may cause large signals, as described in section 5, giving rise to a high energy tail in energy spectra. When APDs were first used this effect was considerable, as can be seen in figure 50, but progress was made rapidly such that the tails seen in 1995 with EG&G APDs were quite small, whilst Hamamatsu APDs were better still, as can be seen in figure 51.

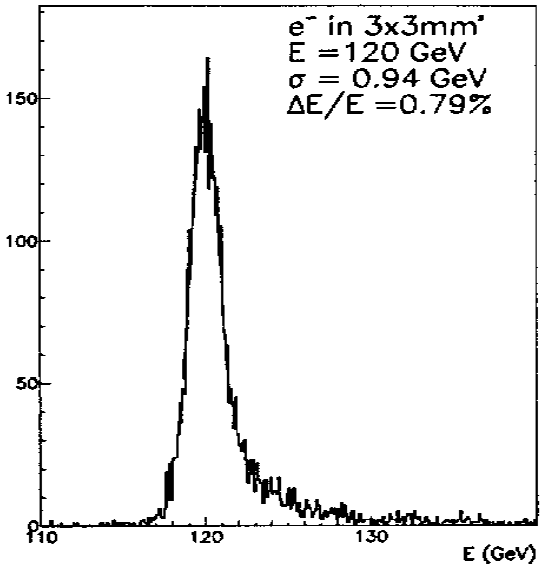

Figure 50: High energy tail seen in 1994 APD

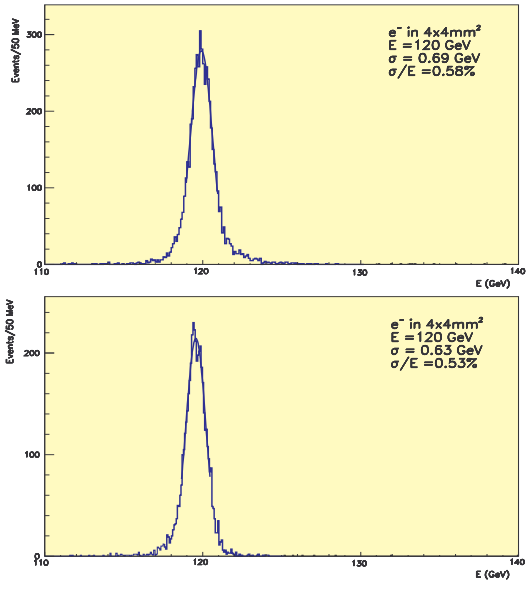

Figure 51: Reduction in high energy tail in 1995 for EG&G APD (top) and Hamamatsu APD (bottom)

APDs from both manufacturers tested in 1996 and 1997 have shown no signs of the nuclear counter effect.

7.4 Energy Resolution

The energy resolution obtained from a 3×3 matrix of crystals has seen a distinct improvement from the first tests made in 1994 when the stochastic term was around 6% and the constant term about 0.6%. The main improvements have been:

- reduction of the nuclear counter effect
- increase in the light yield of the crystals
- improvement in the temperature stability of the containment system
- increase in crystal radiation hardness
- LED monitoring system to 'follow' low-level radiation damage and correct for it

Figure 52 shows the energy resolution measured for 120 GeV electrons incident on 15 different crystals in 1997. The energy is measured in a 3×3 array of crystals centred on the struck crystal. The mean stochastic term is about 4.3% and the mean constant term is about 0.4%. One of the largest contributions to the stochastic term is from photostatistics, which will improve when 2 APDs are used on each crystal. Figure 53 shows the overall energy resolution measured during irradiation up to 650 rads at about 25 rads/hour (similar to the barrel dose at high luminosity) with 120 GeV electrons. The LED system was used to correct for any radiation damage.

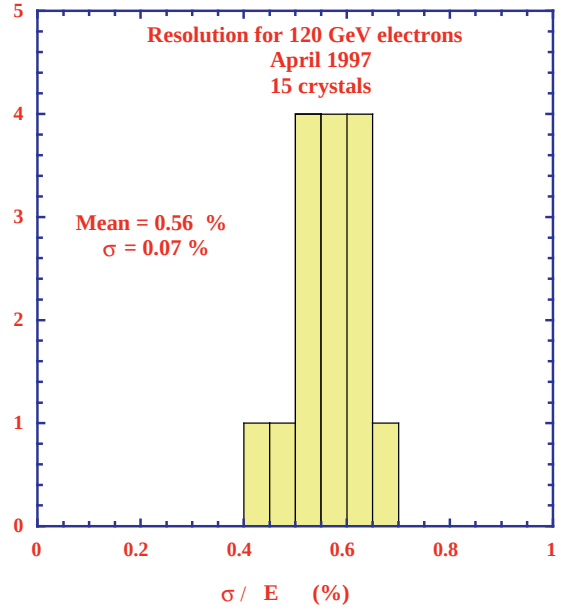

Figure 52: Energy resolution for 120 GeV electrons measured in April 1997

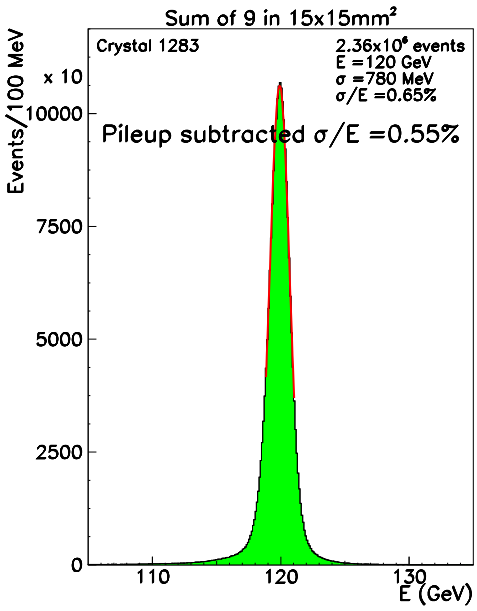

Figure 53: Energy resolution during irradiation up to 650 rads

It should be noted that the energy spectrum in figure 53 is very Gaussian.

7.5 Electron/charged-pion separation

Electrons and charged pions have very different energy spectra, as seen in figure 54, resulting in a large separation factor of the order of a few hundred.

A cut on the transverse shower shape, measured by the crystals, can give a further reduction factor. The overall reduction factor, for a 90% electron efficiency, is around 6000.

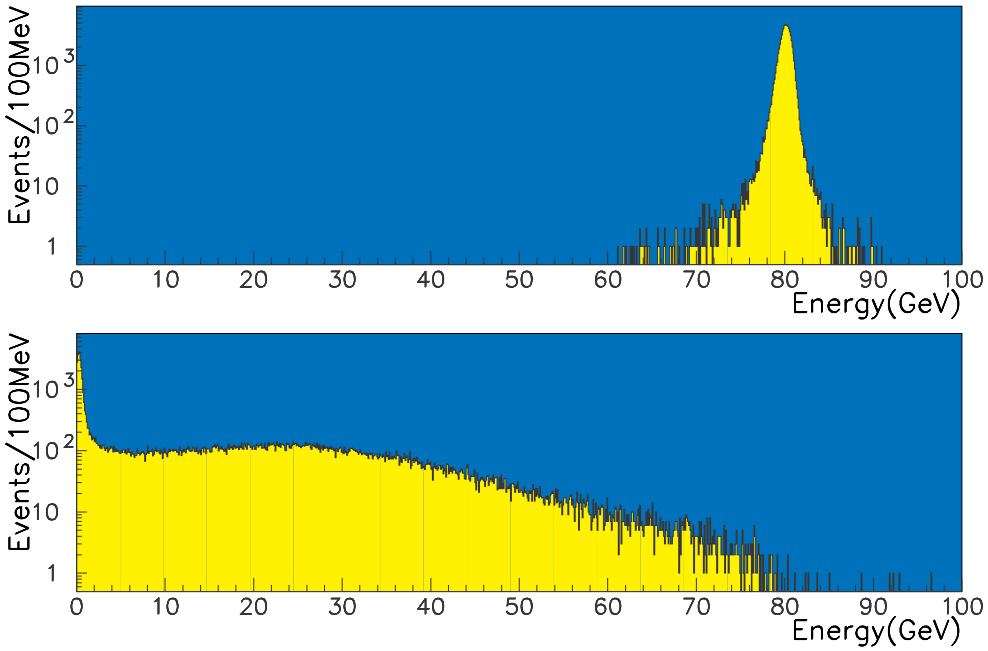

[

Figure 54: 80 GeV electron (top) and π^- (bottom) spectra

7.6 Position and Angular Resolution

The quantity used to define the shower position in the ECAL is the centre of gravity, defined as:

$$X_{cog} = \frac{\sum E_i x_i}{\sum E_i} \tag{10}$$

with the sums running over a 3×3 array of crystals. Since the lateral shower shape is not triangular this estimator is biased and must be corrected. The correction function is derived from the data. The corrected position resolution is shown in figure 55 as a function of incident electron energy.

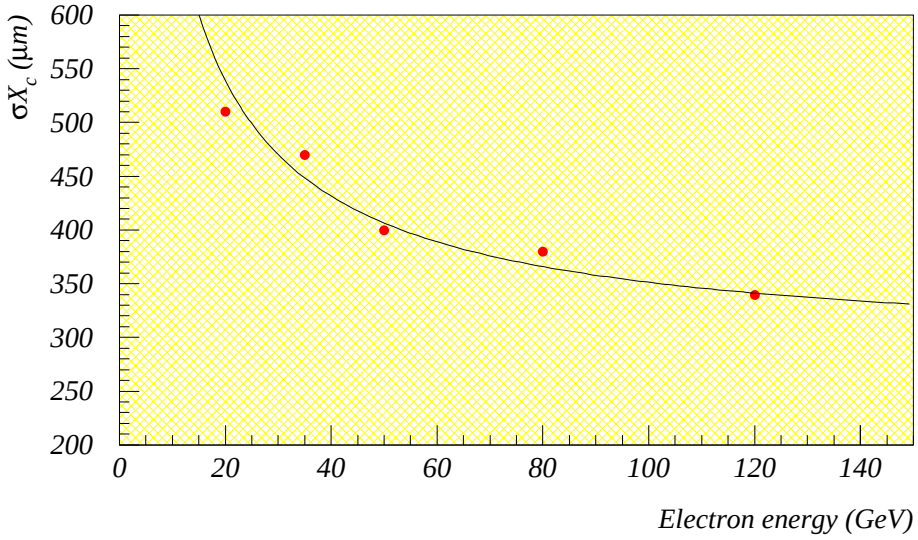

Figure 55: Position resolution of crystals as a function of incident electron energy

The results can be parameterized as:

$$\sigma X_c(mm) = \frac{2.02}{\sqrt{E}} \oplus 0.29 \tag{11}$$

The position resolution for particles incident at an angle relative to the crystal axis is worse than for normally incident particles because fluctuations in the depth of the shower are given a transverse component. This effect is more pronounced for photons than for electrons.

The position measurement in the crystals can be used in conjunction with a position measurement made by the preshower to enable the particle angle of incidence to be estimated. Figure 56 shows the angular resolution measured in the testbeam as a function of incident electron energy. The angular resolution can be parameterized as:

$$\sigma\theta(mrad) = \frac{36.5}{\sqrt{E}} \oplus 4.1 \tag{12}$$

Recent simulation results have confirmed that this order of precision should be obtainable for photons in the barrel of CMS if the barrel preshower is included.

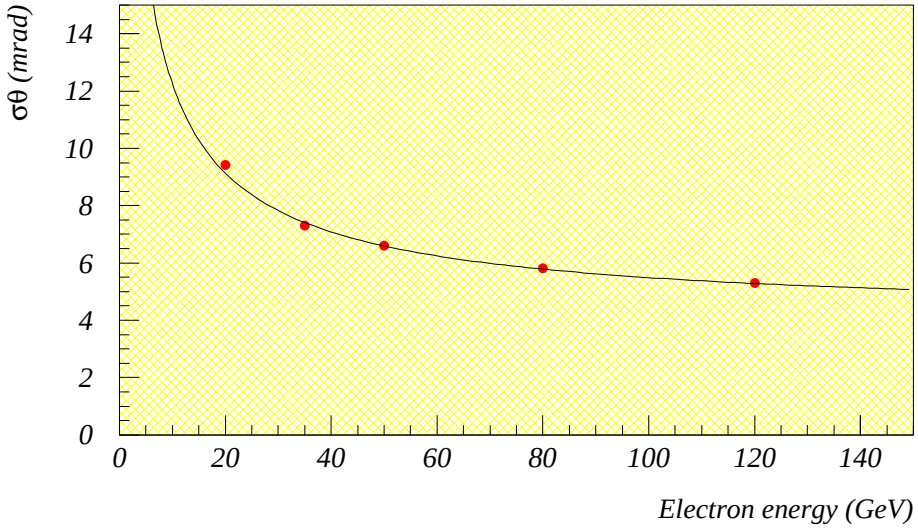

Figure 56: Angular resolution of crystal-preshower system as a function of incident electron energy

8 Current Status and Future Work

The latter half of 1997 saw some major changes to the geometrical design of the CMS ECAL, principally imposed due to cost constraints. This has not compromised the physics performance. This report represents the status of the CMS ECAL at the time of the Gomel school, before these changes had been made. Therefore some details presented in this report are now inaccurate.

The principle change has been to reduce the number of crystals in the ECAL by increasing their lateral dimensions by about 20%. The inner radius of the ECAL has also been reduced, and the layout of 'basket 4' (the barrel ECAL basket at the highest η) has been simplified at the expense of removing the allowed region for the installation of the barrel preshower. Current thoughts are to remove the outermost layer of MSGCs from the tracker and install the barrel preshower in this region if required at high luminosity.

In December of 1997 the ECAL Technical Design Report was submitted to the Large Hadron Collider Committee. The TDR contains the most current ECAL design and performance characteristics, and is generally available from the CMS secretariat.

9 Acknowledgements

This report is a summary of work performed by all the people involved with the CMS ECAL. I would like to particularly thank Etienette Auffray for supplying many of the diagrams used in the 'crystal' section. Philippe Bloch, Michel Della Negra, Jim Virdee and Chris Seez also deserve thanks for their advice and help in compiling this presentation.

Finally, I would like to gratefully acknowledge the incredible hospitality of our hosts in Gomel, particularly Prof. Nikolai Skatchkov and Prof. Nikolai Shumeiko. It was a pleasure to be invited to Gomel, a pleasure which I hope will be repeated.

References

[1] The CMS Collaboration, *"The Electromagnetic Calorimeter Project - Technical Design Report"*, **CERN/LHCC 97-33**.

[2] W. Hoffman *et al.*, Nucl. Instr. and Meth. **A163**, 77 (1979).

[3] J.D.Jackson, *"Classical Electrodynamics"*, 2nd edition, (John Wiley & sons, New York, 1975).

[4] M.A.Akrawy *et al.*, Nucl. Instr. and Meth. **A290**, 76 (1990).

[5] J.B. Birks, *"The Theory and Practice of Scintillation Counting"*, (Pergamon, London, 1964).

[6] B. Rossi, *"High Energy Particles"*, (Prentice-Hall Inc., Englewood Cliffs, NJ, 1952).

[7] The CMS Collaboration, *"The Compact Muon Solenoid - Technical Proposal"*, **CERN/LHCC 94-38**.

[8] A.N.Annenkov et al, *"Systematic Study of the PbWO4 Crystal Short Term Instalibity Under Irradiation"*, **CMS-NOTE/1997-055**